ROMA TRE
UNIVERSITÀ DEGLI STUDI

Dipartimento di Matematica e Fisica
scuola dottorale di Fisica

Atmospheric neutrino spectrum reconstruction with the JUNO experiment

Candidate:
Giulio Settanta

Advisor:
Prof. Stefano Maria Mari

XXXII PhD cycle

This page is intentionally left blank

Contents

Introduction

Neutrinos are elementary particles which are copiously produced through a great variety of processes. Since their first observation in the '50s, experimental efforts have continuously evolved, to find new and more effective ways to detect them. Among the many production channels, the atmospheric neutrino flux represents a well established source that has been used throughout the years to infer important properties of matter at fundamental level. Being produced in the interaction of cosmic radiation with the atmosphere, they are also a probe for nuclear interactions between the air and Cosmic Rays.
Neutrinos have extremely low cross sections, compared to other particles. This peculiar property allows them to preserve the original information at the production and to release it inside a detector without being deflected, nor absorbed. This represents both an advantage and a great experimental challenge. Given the relatively low interaction rate, the only way to detect atmospheric neutrinos is to build huge apparatuses underground, in order to collect a significant statistics and to shield against the atmospheric muon flux, which is much higher.
The JUNO detector, whose site construction started in 2015, was designed with the goal to identify the neutrino mass ordering, by accurately measure the energy spectrum of antineutrinos coming from a surrounding cluster of nuclear power plants. It consist of a 20 kt, $\sim$36 m diameter, spherical volume of liquid scintillator, surrounded by a cosmic muon veto system. The detector is still under construction at a depth of $\sim$700 m and will be ready in 2021. The high light yield of the scintillator and its optimal transparency, together with the high photo-coverage, allow the measurement of the deposited energy with unprecedented resolution. JUNO is expected to take data for more than 20 years and the potentiality of the detector ranges on a wide series of studies.

In this work, the possibility of the JUNO detector in measuring the atmospheric neutrino energy spectrum has been evaluated. A large set of Monte Carlo events has been used to simulate the performances of the detector. The equivalent of $\sim$5 years of data-taking has also been simulated, in order

to understand the detector potential on a reasonable time-scale.
Chapter 1 gives a brief overview of the current knowledge of neutrino physics, both in the framework of the Standard Model and beyond, with the oscillation phenomenon. Present measurements of the atmospheric neutrino energy spectrum are reported in Chapter 2. Chapter 3 describes the final design of the JUNO experiment. Chapter 4 reports the details of the Monte Carlo simulations used. In Chapter 5 are described the selection criteria adopted, while in Chapter 6 the spectrum analysis is presented and discussed, together with the results obtained.

Chapter 1

Atmospheric neutrinos

Atmospheric neutrinos are produced as a result of the interaction of primary Cosmic Rays (CR) with the nuclei of the Earth atmosphere. The primary cosmic ray flux is mainly composed of protons, helium nuclei and a small fraction of heavier nuclei. Being the result of relativistic acceleration, they are not thermalized at the source and their energy distribution follows, at first order, a power-law spectrum: $dN/dE \propto E^{-\gamma}$. The value of γ varies across the spectrum: it is approximately 2.7 up to the PeV, then it increases up to $\approx$3.0 (*knee*). Above the EeV, the value returns around 2.7 (*ankle*). The interaction between primary CR and the Earth's atmosphere produces a cascade of particles known as Extensive Air Shower (EAS), as a result of the air nuclei fragmentation. An EAS is therefore composed of lighter nuclei and secondary hadrons, which undergo re-interactions and decays. Within the shower, neutrinos are produced from the decay of secondary hadrons (mainly pions). Their energy distribution follows approximately that of primary CR. Above energies around $\mathcal{O}(100\ MeV)$, they represent the most abundant natural neutrino flux, up to $\mathcal{O}(100\ TeV)$.
Thanks to the high flux extending over a wide energy range, atmospheric neutrinos represent a natural source that can be used to infer neutrino properties at fundamental level. The discovery of neutrino oscillations, which led to the 2015 Physics Nobel Prize to A. McDonald and T. Kajita, was achieved by analyzing the deficit both in the solar and in the atmospheric neutrino flux. Moreover, some of the missing pieces in the puzzle of neutrino physics, like the mass ordering, are going to be addressed also by means of atmospheric neutrinos. The field is currently very active and several experiments are scheduled in the next years to answer the still open issues.

1.1 Neutrinos in the Standard Model

The original idea of including a neutral, low-mass particle that weakly interacts with matter comes from a letter of W. Pauli to a physics conference at Tubingen in 1930. The elusive fermion, as Pauli explained, could solve some observed experimental anomalies at the time, such as the continuous β spectrum of the neutron decay [1].
The building block of a comprehensive theory that included neutrinos resides in the Fermi theory of β-decays, published in 1934 [2]. In the Fermi formulation, the β decays were described as a point-like interactions between four particles: a proton, a neutron, an electron and a neutrino[1]. Those particles involved in the interaction are called *fermions* and share the property of having a spin value equal to 1/2. Fermi concluded also that neutrinos could be massless.
In the case of the β decay of nucleons, the hamiltonian of the Fermi interaction can be written as

$$H_F^{int} = \frac{G_F}{\sqrt{2}} \sum_J \int d^3x \; c_J \; (\overline{p}(x) O_J n(x) \overline{e}(x) O_J \nu(x) + h.c.), \tag{1.1}$$

where G_F is the Fermi constant[2], c_J are the coefficients of the sum, p,n,e and ν are the four leptonic fields and $h.c.$ is the conjugate hermitian of the expression. O_J refers to the type of coupling the fields can have, being it scalar ($O_S = 1$), axial vector ($O_A = \gamma^\mu\gamma_5$), vector ($O_V = \gamma^\mu$), pseudoscalar ($O_P = \gamma_5$) or tensorial ($O_T = \sigma^{\mu\nu}$). γ_μ are the 4x4 Dirac matrices, γ_5 is the product of the four γ^μ and $\sigma^{\mu\nu} = \frac{i}{2}[\gamma^\mu, \gamma^\nu]$. Several experiments at the time attempted to understand which of the couplings entered in the interaction. A clear picture was missing for about two decades [5]. Meanwhile, at the end of the 30's, it was proposed that weak interactions were mediated by a massive charged boson [6]. In this formulation, the hamiltonian can be written as [7]:

$$H_{IVB} = g_W J^\mu(x) W_\mu^\dagger(x) + g_W J^{\mu\dagger}(x) W_\mu(x), \tag{1.2}$$

where g_W is a dimensionless coupling constant and the W fields represent the charged massive boson. A possible expression of the leptonic currents J in terms of the quantized leptonic fields is:

$$\begin{aligned} J^\mu(x) &= \sum_\ell \overline{\Psi}_\ell(x) \gamma^\mu (1 - \gamma_5) \Psi_{\nu_\ell}(x) \\ J^{\mu\dagger}(x) &= \sum_\ell \overline{\Psi}_{\nu_\ell}(x) \gamma^\mu (1 - \gamma_5) \Psi_\ell(x), \end{aligned} \tag{1.3}$$

[1] The term *neutrino* was invented by Fermi himself, after the 1932 discovery of the neutron by Chadwick [3].

[2] $G_F/(\hbar c)^3 = 1.1663787(6) \times 10^{-5} \; GeV^{-2}$ [4]

where ℓ labels the lepton fields ($\ell = e, \mu, \tau$) and ν_ℓ the corresponding flavor neutrino fields. The structure of (1.2) conserves the so-called *lepton number*, defined as the number of leptons minus the number of antileptons of corresponding flavor. Indeed, the upper current in (1.3) is linear in ℓ creation and in $\overline{\ell}$ absorption creator, same as in ν absorption and in $\overline{\nu}$ creation. Lepton number conservation is today verified experimentally for all processes.
The interaction in (1.2) and (1.3) is also known as 'V - A' interaction, since it can be expressed as the combination of a vector (γ^μ) and an axial vector ($\gamma^\mu\gamma_5$) term:

$$J^\mu(x) = J^\mu_V(x) - J^\mu_A(x). \tag{1.4}$$

It is remarkable to see that such interaction does not conserve parity, since under the transformation $(x,t) \rightarrow (-x,t)$ $J^\mu_V(x)$ changes sign, while J^μ_A(x) does not. Several experimental evidences suggested that parity was not conserved in weak interactions, also within the hadronic sector [8]. In 1957, parity violation was observed in the β-decay of polarized ^{60}Co [9], strengthening the V - A picture.
Another property of neutrinos is given by the *helicity* operator:

$$h = \frac{\overrightarrow{s} \cdot \overrightarrow{p}}{|\overrightarrow{p}|}, \tag{1.5}$$

where $\overrightarrow{s}$ and $\overrightarrow{p}$ are the neutrino spin and momentum vectors. In 1958 it was found that the polarization of ν_e produced in the reaction $e^- + {}^{152}Eu \rightarrow {}^{152}Sm + \nu_e$ was in a direction opposite to its motion, within the experimental uncertainties [10]. The conclusion was that the experiment agreed with the assumption of neutrino as a massless particle, always into an helicity eigenstate. Experimentally, only neutrinos with h = -1 and antineutrinos with h = 1 have been indeed observed so far. Helicity is therefore a conserved quantity and coincides with *chirality*, which governs the interactions with the other particles. The two chiral operators, representing right- and left-handed eigenstates, can be expressed for the fermion field Ψ as:

$$\frac{1 \pm \gamma_5}{2}\Psi. \tag{1.6}$$

In this picture neutrinos always interact as left-handed particles (ν_L) and antineutrinos always as right-handed particles ($\overline{\nu}_R$).
The above statement, about the existence of ν_L and $\overline{\nu}_R$ only, refers to the so-called Dirac representation. If a non-zero neutrino mass is considered, then helicity is not a conserved number and ν and $\overline{\nu}$ can be found in both helicity states. An alternative hypothesis, made by Majorana, is that ν and

$\overline{\nu}$ consist of the same particle, with two different helicity states. As a consequence, the leptonic number would be violated. Several experiments are attempting to investigate this intricate topic, searching for the so-called neutrinoless double-beta decay [11].
The current theoretical picture, where neutrinos are embedded, was formulated in 1967 by Weinberg [12] and Salam [13], based on the $SU(2) \times U(1)$ gauge model proposed in 1961 by Glashow [14]. The new theory, called *Electro-weak Standard Model*, unifies the weak and the electro-magnetic interactions and predicts the existence of a neutral vector boson Z^0. Processes involving the exchange of a Z^0 are called *neutral current* (NC) interactions, to be distinguished from *charged current* (CC) interactions arising from the exchange of a $W^{\pm}$. The existence of NC interactions was proven experimentally in 1973 [15–17].
In the Standard Model (SM) formulation, leptons are divided into left-handed doublets and right-handed singlets (since there are no right-handed neutrinos):

$$\begin{pmatrix} \nu_e \\ e \end{pmatrix}_L \begin{pmatrix} \nu_\mu \\ \mu \end{pmatrix}_L \begin{pmatrix} \nu_\tau \\ \tau \end{pmatrix}_L \quad , \quad e_R \; \mu_R \; \tau_R, \tag{1.7}$$

which explicitly show the $SU(2)$ structure. The resulting Lagrangian density contains three generators for $SU(2)$ and one for $U(1)$. Their mixing creates two charged mediators (the $W^{\pm}$ bosons) and two neutral mediators (the Z^0 and the photon). In order to give mass to the W and Z bosons, the scalar Higgs field induces a mechanisms that breaks the electro-weak symmetry, by allowing the bosons to acquire additional degrees of freedom [18–20]. Massive mediators have a limited range of action, which makes their exchange rather different from the one of the massless photon. At low energy, a weak process can be seen as a point-like interaction, as in the original Fermi formulation.

The experimental confirmation to neutrino existence came in 1956, by the Reines and Cowan experiment at the Savannah River reactor [21]. The apparatus included more than 1000 liters of liquid scintillator, used to detect secondary products after a neutrino interaction. By taking advantage of the large $\overline{\nu}_e$ flux from the nuclear reactor, they used the *inverse β-decay* (IBD) reaction to detect neutrinos: $\overline{\nu}_e + p \rightarrow e^+ + n$. The IBD has a clear signature inside a liquid scintillator, since it produces a prompt energy release after e^+ production and annihilation (few ns) and a delayed one after neutron capture (hundreds of μs).
In the '60s, the first natural flux of neutrinos was experimentally observed: atmospheric neutrinos, resulting from CR interaction in the atmosphere, are able to cross the entire Earth, while atmospheric muons are limited in range

to a few km. By installing multiple detectors inside a deep mine, a signal from neutrino-induced muons created in the surrounding rocks was detected [22, 23].

1.1.1 Neutrino interactions

In the current picture of the SM, neutrinos are included with their 3 flavors representation (ν_e, ν_μ, ν_τ and the corresponding antiparticles). The property of being massless particles imposes that flavor is the only representation they can have. The flavor of a neutrino is defined as that of the charged lepton they couple with in a CC interaction (e, μ, τ).
The only fundamental force they experience is the weak one, via the exchange of the W and Z bosons. The Lagrangian of the CC term has the form

$$\mathcal{L}^{CC} = -\frac{g}{2\sqrt{2}} \sum_{\ell=e,\mu,\tau} (\overline{\nu}_\ell \gamma^\mu \left(1-\gamma^5\right) e_\ell W_\mu + \text{h.c.}), \tag{1.8}$$

where the constant g determines the strength of the coupling. The term in the brackets transforms charged leptons e_ℓ into neutrinos of the same flavor ν_ℓ and vice versa. Concerning the NC term, the lagrangian can be expressed as

$$\begin{aligned}\mathcal{L}^{\text{NC}} = -\frac{g}{4c_\text{W}} \sum_{\ell=e,\mu,\tau} \{&\overline{\nu}_\ell \gamma^\mu \left(1-\gamma^5\right) \nu_\ell - \left(1-2s^2_\text{W}\right) \overline{e}_\ell \gamma^\mu \left(1-\gamma^5\right) e_\ell \\ &+ 2s^2_\text{W} \overline{e}_\ell \gamma^\mu \left(1+\gamma^5\right) e_\ell\} Z_\mu,\end{aligned} \tag{1.9}$$

where s_W and c_W are the sine and cosine of the weak mixing angle θ_W. The two processes are reported in terms of Feynman diagrams in fig 1.1.

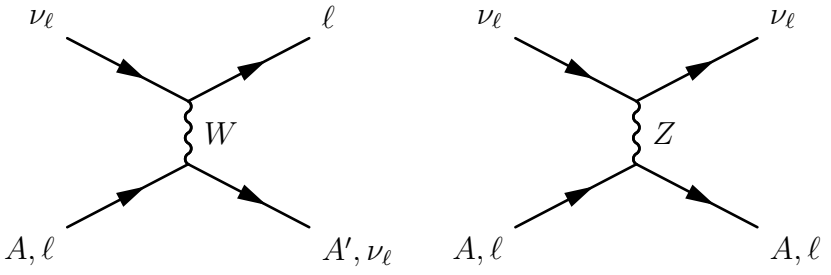

Figure 1.1: Feynman diagrams for neutrino interactions with generic hadrons or leptons. Left: charged-current (CC) interactions; right: neutral-current (NC) interactions. ν_ℓ denotes neutrinos, A hadrons, ℓ charged leptons.

The treatment of neutrino interactions in not trivial, because of the multiplicity of possible targets. Therefore, it is convenient to address the is-

sue on distinct regions of the parameter space, where some approximations can be done. In the energy region considered in this work, about $100\,MeV \leq E_\nu \leq 10\,GeV$, the dominant neutrino interaction is the neutrino-nucleon scattering. The most prominent channels, which are described below, are the *elastic* and *quasi-elastic* scattering, the *resonant production* and the *deep inelastic* scattering. More details on the processes and their implementation in the neutrino event generator are in Chap. 4. The treatment here follows the review work from [5] and [24].

Elastic and quasi-elastic scattering : Neutrinos can elastically scatter off an entire nucleon, delivering a nucleon (or multiple nucleons) from the target. In the case of CC neutrino scattering, this process is referred to as "quasi-elastic scattering", whereas for NC scattering this is traditionally referred to as "elastic scattering". In the approximation of $E_\nu << 1\,GeV$, the total cross-section for quasi-elastic scattering can be expressed as

$$\sigma_{\mathrm{CC}} \simeq 1.601 \times 10^{-44} \left(1 + 3g_A^2\right) \left(\frac{E_\nu}{\mathrm{MeV}}\right)^2 \mathrm{cm}^2, \tag{1.10}$$

where g_A is the coefficient of the axial contribution. In the same approximation, the total cross-section for elastic scattering is given by

$$\begin{aligned} \sigma^p_{\mathrm{NC}} &\simeq \frac{G_{\mathrm{F}}^2}{4\pi} \left[\left(1 - 4\sin^2\vartheta_{\mathrm{W}}\right)^2 + 3g_A^2\right] E_\nu^2 \\ \sigma^n_{\mathrm{NC}} &\simeq \frac{G_{\mathrm{F}}^2}{4\pi} \left[1 + 3g_A^2\right] E_\nu^2, \end{aligned} \tag{1.11}$$

where the superscript p refers to the interaction with a proton and n with a neutron. The ratio $\sigma_{\mathrm{NC}}/\sigma_{\mathrm{CC}}$ has been measured around a value of (0.1 - 0.15) [24].

Resonance production : Neutrinos can excite the target nucleon to a resonance state. The resultant baryonic resonance $N^\star$ decays to a variety of possible mesonic final states, resulting in a combination of nucleons and mesons. The most abundant products are pions, which can appear in single-production or in a certain multiplicity.

Deep-inelastic scattering : At high enough energy, neutrinos can resolve the individual quark constituents of the nucleon. The interaction is thus able to destroy the nucleon and manifests in the creation of a hadronic shower. The process is described in terms of the *quark-parton* model of hadrons, where a nucleon is considered as a combination of

three valence quarks, plus a sea of gluons and quark-antiquark pairs. The interaction probability with any of the parton depends on the probability density $f_{q_i}^N(x)$, which describes the probability of finding a specific quark q_i. A set of variables that are useful to describe the process are the momentum transfer Q^2, the inelasticity $y \equiv 1-(E_\ell/E_\nu)$ (being E_ℓ and E_ν the energy of the charged lepton and of the neutrino and $-Q^2 = q^2$), the center-of-mass energy s and $x \equiv Q^2/(s-m_N^2)$. All these variables are invariant under Lorentz transformation.
The differential cross-section for CC interactions can be expressed as:

$$\begin{aligned} \frac{\mathrm{d}^2\sigma_{\mathrm{CC}}^{\nu N}}{\mathrm{d}x\mathrm{d}y} &= 2x\sigma_{\mathrm{CC}}^0 \left[\sum_{q=d,s} f_q^N(x) + (1-y)^2 \sum_{\overline{q}=\overline{u},\overline{c}} f_{\overline{q}}^N(x) \right] \\ \frac{\mathrm{d}^2\sigma_{\mathrm{CC}}^{\overline{\nu} N}}{\mathrm{d}x\mathrm{d}y} &= 2x\sigma_{\mathrm{CC}}^0 \left[\sum_{\overline{q}=\overline{d},\overline{s}} f_{\overline{q}}^N(x) + (1-y)^2 \sum_{q=u,c} f_q^N(x) \right], \end{aligned} \tag{1.12}$$

assuming the existence of the first two quark generations only and that the target nucleus has an equal number of protons and neutrons. The parameter σ_{CC}^0 is given by

$$\sigma_{\mathrm{CC}}^0 = \frac{G_{\mathrm{F}}^2}{2\pi} s \left(1 + \frac{Q^2}{m_W^2} \right)^{-2}, \tag{1.13}$$

where m_W is the W boson mass. A similar expression can be derived for NC interactions and the relationship between σ^{NC} and σ^{CC} depends on the weak mixing angle only:

$$\frac{\sigma_{\mathrm{NC}}^{\nu} - \sigma_{\mathrm{NC}}^{\overline{\nu}}}{\sigma_{\mathrm{CC}}^{\nu} - \sigma_{\mathrm{CC}}^{\overline{\nu}}} = \frac{1}{2}\left(1 - \sin^2\vartheta_{\mathrm{W}}\right), \tag{1.14}$$

where the superscript ν and $\overline{\nu}$ refers to the interaction of neutrinos or antineutrinos.

The energy region considered in this work is often referred to as *transition region*, since the theoretical approach goes from the assumption of nucleons as a whole to the free-parton approximation at higher energies. Furthermore, most of the difficulties in the associated measurements arise from the final-state interactions, since secondary particles are often produced within the nuclei and experience further interactions before coming out. Presently, main experimental contributions come from accelerator-based measurements, which can provide a lot of information about neutrino interactions on a great variety of targets. Some measurements of the inclusive cross section of ν_μ

and $\overline{\nu}_\mu$ are reported on fig. 1.2, where a linear energy dependence is evident above $E_\nu \approx 10\,\text{GeV}$, confirming the validity of the *quark-parton* model. A linear behaviour is indeed expected in the assumption of point-like scattering of neutrinos from quarks, which is no longer valid at low energies.

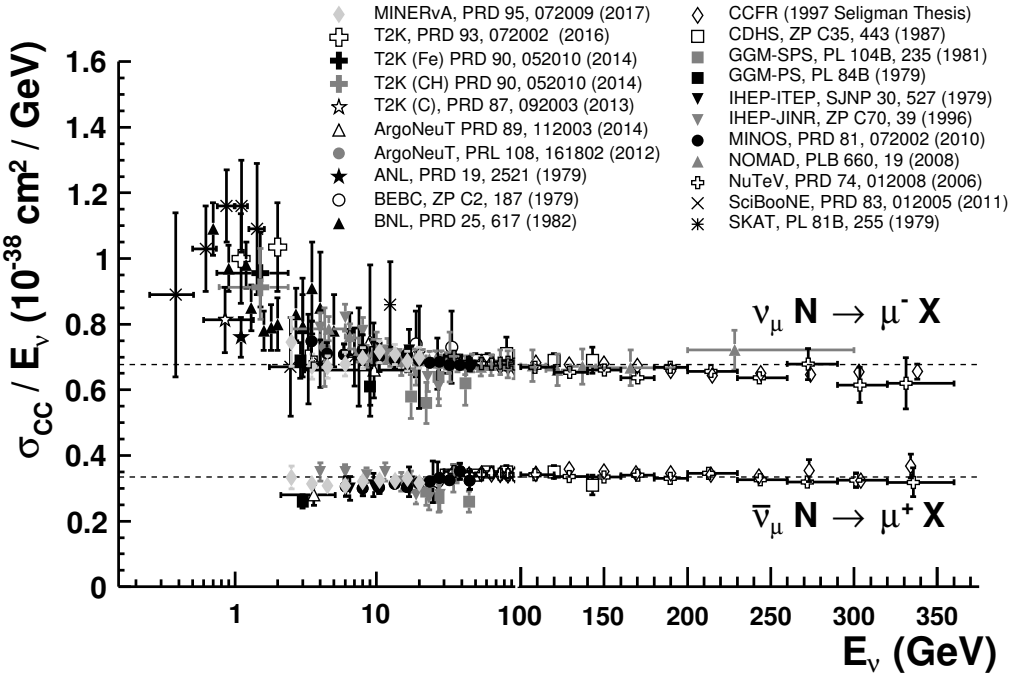

Figure 1.2: Measurements of per nucleon ν_μ and $\overline{\nu}_\mu$ CC inclusive scattering cross section, divided by neutrino energy, as a function of neutrino energy. At $E_\nu = 100\,\text{GeV}$ the scale transits from logarithmic to linear. Figure from [4].

1.2 Neutrino oscillation

The term *neutrino oscillation* refers to the phenomenon of neutrino flavor changing during propagation. This is a relatively recent discovery, which had an impressive influence in particle physics, and its description needs an extension of the SM.

Neutrinos produced in a flavor eigenstate have a nonzero probability to be found with a different flavor after a certain distance. The mechanism of oscillations was first suggested by Pontecorvo [25] and has been explained by the fact that neutrinos do have mass. Apart from the representation chosen,

the theory of neutrino oscillation in vacuum can be briefly outlined starting from two basic assumptions:

- there are $j = 3$ neutrino mass eigenstates $|\nu_1\rangle$, $|\nu_2\rangle$, $|\nu_3\rangle$;
- the $\alpha = 3$ flavor eigenstates $|\nu_e\rangle$, $|\nu_\mu\rangle$, $|\nu_\tau\rangle$ do not correspond to the mass eigenstates.

Neutrinos are produced in charged-current weak interactions in association with a charged lepton, as flavor eigenstates, but propagate as mass eigenstates. The weak eigenstates α do not have a one-to-one correspondence to the mass eigenstates j and can be expressed as a linear combination of them[3]:

$$|\nu_\alpha\rangle = \sum_j U^*_{\alpha j} \, |\nu_j\rangle. \tag{1.15}$$

U is the 3×3 unitary Pontecorvo-Maki-Nakagawa-Sakata (PMNS) matrix [25, 26]:

$$\begin{pmatrix} \nu_e \\ \nu_\mu \\ \nu_\tau \end{pmatrix} = \begin{pmatrix} U_{e1} & U_{e2} & U_{e3} \\ U_{\mu 1} & U_{\mu 2} & U_{\mu 3} \\ U_{\tau 1} & U_{\tau 2} & U_{\tau 3} \end{pmatrix} \begin{pmatrix} \nu_1 \\ \nu_2 \\ \nu_3 \end{pmatrix} \tag{1.16}$$

and connects the flavor with the mass eigenstates, as a rotation in the two bases space. Anti-particles can be described by the conjugate matrix. In general, a 3×3 complex matrix has $2N^2 = 18$ independent parameters. The unitarity constraint and a convenient choice of the complex phases reduces the number of independent parameters to 4: 3 real numbers and 1 complex phase. Two additional phase parameters can be introduced if neutrinos are Majorana particles.
The U matrix can be therefore expressed as

$$U = \begin{pmatrix} 1 & 0 & 0 \\ 0 & c_{23} & s_{23} \\ 0 & -s_{23} & c_{23} \end{pmatrix} \times \begin{pmatrix} c_{13} & 0 & e^{-i\delta} s_{13} \\ 0 & 1 & 0 \\ -e^{-i\delta} s_{13} & 0 & c_{13} \end{pmatrix} \times \begin{pmatrix} c_{12} & s_{12} & 0 \\ -s_{12} & c_{12} & 0 \\ 0 & 0 & 1 \end{pmatrix} \times \begin{pmatrix} e^{i\rho_1} & 0 & 0 \\ 0 & e^{i\rho_2} & 0 \\ 0 & 0 & 1 \end{pmatrix}, \tag{1.17}$$

where $s_{jk} \equiv sin\theta_{jk}$ and $c_{jk} \equiv cos\theta_{jk}$. Here the real parameters are the three mixing angles (θ_{12}, θ_{23} and θ_{13}), while δ represents the phase parameter and

[3] The description of neutrino oscillation in this section follows with good approximation that in [5].

is related to the CP violation in the neutrino sector. ρ_1 and ρ_2 refer to the Majorana representation only and do not produce any flavor transformation effect, since they are on-diagonal terms.
The temporal evolution of a flavor eigenstate, produced at time $t = 0$ in the eigenstate $|\nu(t = 0)\rangle \equiv |\nu_\alpha\rangle$, is governed by the Schrödinger equation:

$$i\frac{d}{dt}|\nu_\alpha\rangle = \mathcal{H}|\nu_\alpha\rangle, \tag{1.18}$$

where $\mathcal{H}$ is the hamiltonian of the system.
The neutrino energy for a flavor eigenstate is not well defined, since each component has an energy $E_j = \sqrt{p^2 + m_j^2}$. The evolution of each mass eigenstate is thus given by the term $e^{-iE_j t}$ (here assuming $\hbar = c = 1$):

$$|\nu(t)\rangle = \sum_j U^*_{\alpha j} e^{-iE_j t}\ |\nu_j\rangle. \tag{1.19}$$

The probability to observe a neutrino at time t in a flavor eigenstate β, produced at time $t = 0$ in a flavor eigenstate α, is thus:

$$\begin{aligned} P_{\nu_\alpha \to \nu_\beta} = |\langle \nu_\beta | \nu(t)\rangle|^2 &= \left| \sum_j U^*_{\alpha j} U_{\beta j} e^{-iE_j t} \right|^2 \\ &= \sum_{j,k} U^*_{\alpha j} U_{\beta j} U_{\alpha k} U^*_{\beta k} e^{-i(E_j - E_k)t}, \end{aligned} \tag{1.20}$$

which is nonzero for $\beta \neq \alpha$. The small neutrino mass, $\lesssim 1\,\text{eV}$, allows the expansion of the energy expression as:

$$E_i = \sqrt{p^2 + m_i^2} \simeq p + \frac{m_i^2}{2p} \simeq E + \frac{m_i^2}{2E}. \tag{1.21}$$

The exponential term thus becomes:

$$-i(E_j - E_k)t \simeq -i\frac{\Delta m^2_{jk}}{2E} t \simeq -i\frac{\Delta m^2_{jk}}{2E} L, \tag{1.22}$$

where L is the propagation baseline and $L \simeq t$ for relativistic neutrinos. $\Delta m^2_{jk} = m_j^2 - m_k^2$ is the squared mass difference between the $|\nu_j\rangle$ and the $|\nu_k\rangle$ eigenstates. By replacing (1.22) in (1.20), the transition probability

becomes:

$$\begin{aligned} P_{\nu_\alpha \to \nu_\beta} &= \sum_{j,k} U^*_{\alpha k} U_{\beta k} U_{\alpha j} U^*_{\beta j} e^{-i\frac{\Delta m^2_{kj}}{2E}L} \\ &= \delta_{\alpha\beta} - 4\sum_{j>k} \mathcal{Re}(U^*_{\alpha j} U_{\beta j} U_{\alpha k} U^*_{\beta k})\ sin^2\left(\frac{\Delta m^2_{jk} L}{4E}\right) \\ &\quad \pm 2\sum_{j>k} \mathcal{Im}(U^*_{\alpha j} U_{\beta j} U_{\alpha k} U^*_{\beta k})\ sin\left(\frac{\Delta m^2_{jk} L}{4E}\right), \end{aligned} \tag{1.23}$$

where $\delta_{\alpha\beta}$ is the Kronecker delta function and the sign of the imaginary part depends on whether neutrinos (+) or antineutrinos (-) are considered. The probability in (1.23) depends on the four parameters of the U matrix, the squared mass difference Δm^2_{jk} and the ratio between the propagation distance (called *baseline*) and the neutrino energy L/E. While the latter is determined by the experimental setup, the other parameters are subject to measurements to be determined.
Currently, the value of the three mixing angles and the two squared mass differences have been measured with reasonable precision (table 1.1). There are indications on the value of the δ phase, but with large uncertainties. The *mass hierarchy* (*i.e.* the sign of Δm_{jk}) is still unknown: the heaviest ν_3 hypothesis is commonly addressed as *Normal Hierarchy*, while the heaviest ν_1 as *Inverted Hierarchy* [27].

Parameter	Normal Hierarchy	Inverted Hierarchy
$sin^2\theta_{12}$	$0.297^{+0.057}_{-0.047}$	
$sin^2\theta_{23}$	$0.425^{+0.19}_{-0.044}$	$0.589^{+0.047}_{-0.205}$
$sin^2\theta_{13}$	$0.0215^{+0.0025}_{-0.0025}$	$0.0216^{+0.0026}_{-0.0026}$
$\delta\ /\pi$	$1.38^{+0.52}_{-0.38}$ (2σ)	$1.31^{+0.57}_{-0.39}$ (2σ)
$\Delta m^2_{21}\ /10^{-5}\,eV^2$	$7.37^{+0.59}_{-0.44}$	
$\Delta m^2_{32}\ /\,10^{-3} eV^2$	$2.56^{+0.13}_{-0.12}$	$2.54^{+0.12}_{-0.12}$

Table 1.1: Best-fit neutrino oscillation parameters with associated 3σ experimental uncertainty. Results are given both assuming normal hierarchy and inverted hierarchy. Values are taken from [4].

A useful simplification comes with the so-called *two-neutrino scheme*: by choosing a certain value of the L/E ratio, the experimental setup is sensitive, with good approximation, to a sub-section of the U matrix only. In this case,

U can be be reduced to a 2×2 matrix and only one free parameter θ:

$$\mathbf{U}^{2\nu} = \begin{pmatrix} \cos\theta & \sin\theta \\ -\sin\theta & \cos\theta \end{pmatrix} \tag{1.24}$$

and the flavor transition probability is simply calculated as

$$P^{2\nu}_{\nu_\alpha \to \nu_\beta}(L, E) = \sin^2(2\theta)\sin^2\left(\frac{\Delta m^2}{4E}L\right), \tag{1.25}$$

where $\Delta m^2 \equiv m^2_\beta - m^2_\alpha$ and $\alpha \neq \beta$. The 2ν simplification is an optimal tool for data analysis at first stage, since corrections from full 3ν approach are usually very small.

Matter effects

The presence of matter along neutrino trajectories can influence the oscillation probability. Even if neutrinos rarely interact with matter, the coherent effect of forward scattering from electrons during propagation must be considered. While NC interactions $\nu e \to \nu e$ affect all neutrino flavors in the same way (fig. 1.1, right), ν_e experience CC coherent forward scattering with electrons, resulting in $\nu_e e \to \nu_e e$ (fig. 1.1, left, $\ell = e$). This asimmetry generates a modification of the oscillation scheme. If $E_{\nu_\ell} > m_\ell$, also ν_μ and ν_τ can undergo the same CC interaction, but not in a coherent process.
The effect can be summarized in terms of *effective* oscillation parameters that neutrinos experience during propagation, known as *matter effects* [28]. The net effect of matter is to introduce an effective potential energy term for electron neutrinos:

$$\pm\, V_{MAT} = \sqrt{2} G_F N_e, \tag{1.26}$$

where N_e is the electron number density and the plus or minus sign refers to neutrinos and antineutrinos, respectively. Eq. 1.18 describes the propagation of neutrinos in vacuum. If matter is considered, the total hamiltonian can be expressed as

$$\mathcal{H} = \mathcal{H}_{VAC} + \mathcal{H}_{MAT}. \tag{1.27}$$

The eigenstates of $\mathcal{H}_{VAC}$ are the neutrino mass eigenstates $|\nu_1\rangle$, $|\nu_2\rangle$, $|\nu_3\rangle$. $\mathcal{H}_{MAT}$ describes the interactions between neutrinos and matter, and their eigenstates are the neutrino flavor states. Since only CC scattering of ν_e gives a relevant contribution, the matter term gives:

$$\mathcal{H}_{MAT}|\nu_e\rangle = V_{MAT}|\nu_e\rangle. \tag{1.28}$$

Eq. (1.28) shows that the total hamiltonian is dependent on the electron density N_e, so that the solution in (1.19) is no longer valid.

By defining the flavor transition amplitude $\psi_{\alpha\beta}(t) = \langle\nu_\beta|\nu_\alpha(t)\rangle$, a similar approach as for the vacuum case can be adopted. The amplitude evolution is given by

$$i\frac{d}{dt}\psi_{\alpha\beta}(t) = \left(\sum_j U^*_{\alpha j}\frac{\Delta m^2_{j1}}{2E}U_{\beta j} + \delta_{\alpha e}V_{\rm CC}\right)\psi_{\alpha\beta}(t). \tag{1.29}$$

Eq. (1.29) has the structure of a Schrödinger equation, approximating $t \simeq x$:

$$i\frac{d}{dx}\Psi_\alpha = \mathcal{H}_F\Psi_\alpha, \tag{1.30}$$

with the effective hamiltonian $\mathcal{H}_F$ in the flavor basis given by

$$\mathcal{H}_{\rm F} = \frac{1}{2E}\left(U\mathcal{M}^2U^\dagger + \mathcal{A}\right). \tag{1.31}$$

In the 3ν scheme:

$$\Psi_\alpha = \begin{pmatrix}\psi_{\alpha e}\\ \psi_{\alpha\mu}\\ \psi_{\alpha\tau}\end{pmatrix}, \quad \mathcal{M}^2 = \begin{pmatrix}0 & 0 & 0\\ 0 & \Delta m^2_{21} & 0\\ 0 & 0 & \Delta m^2_{31}\end{pmatrix}, \quad \mathcal{A} = \begin{pmatrix}A_{\rm MAT} & 0 & 0\\ 0 & 0 & 0\\ 0 & 0 & 0\end{pmatrix}, \tag{1.32}$$

where A_{MAT} is given by

$$A_{MAT} = 2EV_{MAT} = 2\sqrt{2}EG_FN_e. \tag{1.33}$$

The amplitude evolution expression in (1.29) can be conveniently expressed in matrix form in the 2ν scheme, by neglecting the τ mixing:

$$i\frac{\rm d}{{\rm d}x}\begin{pmatrix}\psi_{ee}\\ \psi_{e\mu}\end{pmatrix} = \frac{1}{4E}\begin{pmatrix}-\Delta m^2\cos 2\theta + A_{\rm MAT} & \Delta m^2\sin 2\theta\\ \Delta m^2\sin 2\theta & \Delta m^2\cos 2\theta - A_{\rm MAT}\end{pmatrix}\begin{pmatrix}\psi_{ee}\\ \psi_{e\mu}\end{pmatrix}, \tag{1.34}$$

where $\Delta m^2 \equiv m^2_2 - m^2_1$ and θ is the mixing angle, which gives

$$\nu_e = \cos\theta\nu_1 + \sin\theta\nu_2, \quad \nu_\mu = -\sin\theta\nu_1 + \cos\theta\nu_2. \tag{1.35}$$

The evolution equation can always be solved numerically. In case of a matter density profile which is smooth enough, an approximate analytical solution of eq. (1.34) can be obtained. The effective hamiltonian $\mathcal{H}_F$, for the evolution equation in (1.34), has the form

$$\mathcal{H}_{\rm F} = \frac{1}{4E}\begin{pmatrix}-\Delta m^2\cos 2\theta + A_{\rm MAT} & \Delta m^2\sin 2\theta\\ \Delta m^2\sin 2\theta & \Delta m^2\cos 2\theta - A_{\rm MAT}\end{pmatrix} \tag{1.36}$$

and can be diagonalized by the transformation

$$U_{\mathrm{M}}^{T}\mathcal{H}_{\mathrm{F}}U_{\mathrm{M}} = \mathcal{H}_{\mathrm{M}}, \tag{1.37}$$

where

$$\mathcal{H}_{\mathrm{M}} = \frac{1}{4E}\begin{pmatrix} -\Delta m_{M}^{2} & 0 \\ 0 & \Delta m_{M}^{2} \end{pmatrix} \tag{1.38}$$

is the effective hamiltonian in the mass basis in matter. The unitary matrix

$$U_{\mathrm{M}} = \begin{pmatrix} \cos\vartheta_{\mathrm{M}} & \sin\vartheta_{\mathrm{M}} \\ -\sin\vartheta_{\mathrm{M}} & \cos\vartheta_{\mathrm{M}} \end{pmatrix} \tag{1.39}$$

represents the effective mixing matrix in matter and the effective squared-mass differences are

$$\Delta m_{\mathrm{M}}^{2} = \sqrt{\left(\Delta m^{2}\cos 2\vartheta - A_{\mathrm{MAT}}\right)^{2} + \left(\Delta m^{2}\sin 2\vartheta\right)^{2}}. \tag{1.40}$$

The effective mixing angle in the U_M matrix is finally given by

$$\tan\left(2\theta_{\mathrm{M}}\right) = \tan(2\theta)/\left(1 - \frac{A_{MAT}}{\Delta m^{2}\cos(2\theta)}\right). \tag{1.41}$$

Given the form of the (1.41), it is evident that oscillation effects in matter can become maximal: if the matter potential has the value

$$A_{\mathrm{MAT}} = \Delta m^{2}\cos(2\theta) \tag{1.42}$$

the tangent function goes to infinite and the effective mixing angle is equal to $\pi/4$, leading to a maximal mixing. This resonant enhancement is known as *MSW effect* , named after Wolfenstein [28] and Mikheyev and Smirnov [29]. Eq. (1.42) implies also that, in order to achieve the resonant condition for neutrinos, the signs of Δm^2 and $cos(2\theta)$ must be equal. For antineutrinos, they must be opposite. Therefore, the observation of the MSW effect for neutrinos or antineutrinos is a way to test the ordering of neutrino masses. In the case of atmospheric neutrinos, the passage through matter brings to an enhancement of the small mixing angle θ_{13}.

1.3 Atmospheric neutrino flux

The atmospheric neutrino flux is one of the secondary components which originate from the interaction of the cosmic ray flux with the Earth's atmosphere. The primary component of CR is composed of protons at 90%, alpha

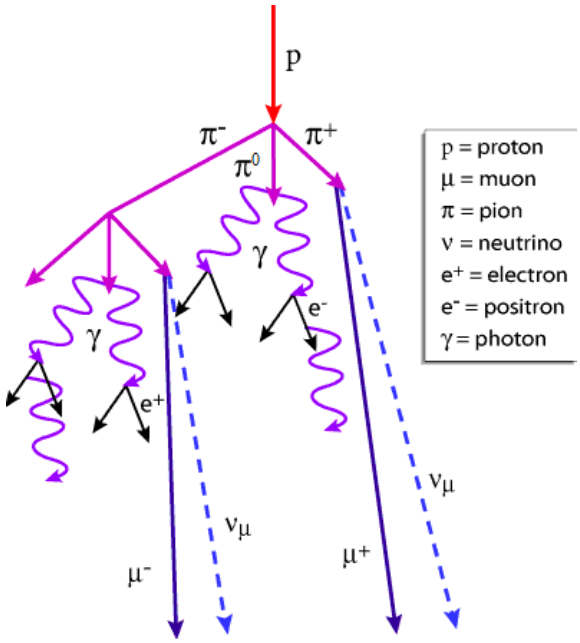

Figure 1.3: Schematic view of the air shower formation after a proton interaction. The pion component is highlighted.

particles at 9% and heavier nuclei for the rest. The collisions between cosmic ray particles and air molecules generate a cascade of secondary hadrons, mainly pions. These hadrons either re-interact or decay, producing further particles, which accumulate and form a relativistic disk called *air shower*. A sketch of the process is shown in fig. 1.3. The pions produced within the shower decay predominantly into muons and muon neutrinos:

$$\pi^{\pm} \rightarrow \mu^{\pm} + \overset{(-)}{\nu}_{\mu}. \tag{1.43}$$

For K mesons the same process occurs, but their contribution becomes relevant at high energies only. Muons which decay in-flight add a further neutrino component, through the process

$$\mu^{\pm} \rightarrow e^{\pm} + \overset{(-)}{\nu}_{e} + \overset{(-)}{\nu}_{\mu}. \tag{1.44}$$

The flux of these atmospheric neutrinos has an energy distribution which, at first order, follows the power-law spectrum of the primary CR: $dN/dE \propto E^{-2.7}$. As for the primary radiation, they are distributed over a wide energy range, from tenth of MeV up to the PeV. Assuming that all particles in (1.43)

and (1.44) undergo the described processes, the neutrino flux satisfies with good approximation the ratios:

$$\frac{\phi_{\nu_\mu} + \phi_{\overline{\nu}_\mu}}{\phi_{\nu_e} + \phi_{\overline{\nu}_e}} \simeq 2, \quad \frac{\phi_{\nu_\mu}}{\phi_{\overline{\nu}_\mu}} \simeq 1, \quad \frac{\phi_{\nu_e}}{\phi_{\overline{\nu}_e}} \simeq \frac{\phi_{\mu^+}}{\phi_{\mu^-}}. \tag{1.45}$$

An accurate approach must consider a full study of the primary cosmic ray flux, the hadronic processes within the cosmic radiation and the atmosphere and the impact of the geomagnetic field.
The atmospheric neutrino flux from the decay of π and K mesons is referred to as *conventional*. At energies above 100 TeV, neutrinos are expected to be produced mainly from the decay of heavier charmed mesons. Given the very short lifetime of such heavy particles, the flux is commonly referred to as *prompt* [30] and so far has not been observed yet.

1.3.1 Monte Carlo flux simulations

In order to simulate a realistic neutrino flux at Earth, some tools and models have been developed throughout the years. At first approach, the atmospheric neutrino flux can be parametrized as

$$\phi_{v_i}(E) = \sum_A \left(\int_0^\infty \phi_A(E') \times R_A(E') \times Y_{A \to v_i}(E', E)\ dE' \right), \tag{1.46}$$

where $\phi_A(E')$ is the spectrum of the primary nucleus A, $R_A(E')$ takes into account the filtering effect of the geomagnetic field for nuleus A and $Y_{A \to v_i}(E', E)$ is the average yield of neutrinos of energy E reaching the ground for a nucleus A with energy E'. In 1-dimensional (1D) calculations, secondary particles are propagated along the same trajectory as that of the primary, neglecting their transverse momenta and the bending due to the geomagnetic field. 3-dimensional (3D) calculations include random directions of the secondaries and are therefore much more CPU and time consuming.
As already mentioned, the geomagnetic field deviates the cosmic charged particles coming from outside, excluding the less energetic ones. An important parameter associated with the geomagnetic effect is the *magnetic rigidity* R, which is the ratio between the total momentum of the particle and its electric charge. The gyroradius of the particle trajectory is therefore linearly dependent of R, so that high-Z nuclei are more subject to deviation than low-Z ones. Particles which have a great deviation never reach the ground, resulting in the so-called *rigidity cutoff*. Since the cutoff depends on the particular nucleus, its effect is also to modify the composition of CR which enters the atmosphere. This nucleus-dependent effect is parametrized by the factor R

in (1.46).
The spectra of the cosmic ray components are measured by many experiments, giving an input to neutrino flux simulations. However, some experimental results are not fully in agreement and therefore several fits can be performed on the spectra. The usage of different fits on the primary spectra, as well as different assumptions on the hadron interaction model, lead to different results on the atmospheric neutrino flux calculations.

The HKKM model

The HKKM model has been released for the first time in the '80s and is continuously mantained and updated [31–34]. The model provides the atmospheric neutrino flux calculation at some geographical locations, corresponding to present neutrino detectors (e.g. Super-Kamiokande, INO, JUNO...). The flux is available online in table format, in terms of energy and direction. The energy range spans from 0.1 to 10^4 GeV.
In the last version [34] the calculation is fully 3D. Primary particles are injected from a sphere with radius $R_{inj} = R_E + 100\,\text{km}$ [4] and the escape sphere with radius $R_{esc} = 10\ R_E$. Primary CR are sampled according to energy and composition and go through the rigidity cutoff. If the primary passes the cutoff, it is propagated through the atmosphere. Each secondary produced in interactions is recursively asked to pass rigidity cutoff, until they reach the escape sphere, or hit the surface of the Earth, or interact with an air nucleus, or decay. The key parameter which drives the geomagnetic effects is the horizontal component of the geomagnetic field, which is reported in fig. 1.4. In the HKKM model, the solar modulation is also considered.
The produced neutrino paths are sampled around the detector site, so that, if it crosses the detector surface, it is considered in the flux calculation. Instead of the real detector dimensions, a circular virtual detector surface with radius of 1113.2 km is used. Then, a correction is applied to take into account the real detector size.
Seasonal differences in the flux are taken into account, but they are computed to be very small at mid-latitude and tropical regions (like JUNO). Asymmetry effects in the azimuthal distribution of neutrinos are also considered.
The total error on the HKKM calculation is estimated to be lower than 10% between 1 and 10 GeV and higher outside this region. Uncertainties include the atmospheric density profile, neutrino cross-section, π and K fluxes.

[4] $R_E = 6378.140\,\text{km}$ is the Earth radius, assumed to be perfectly spherical.

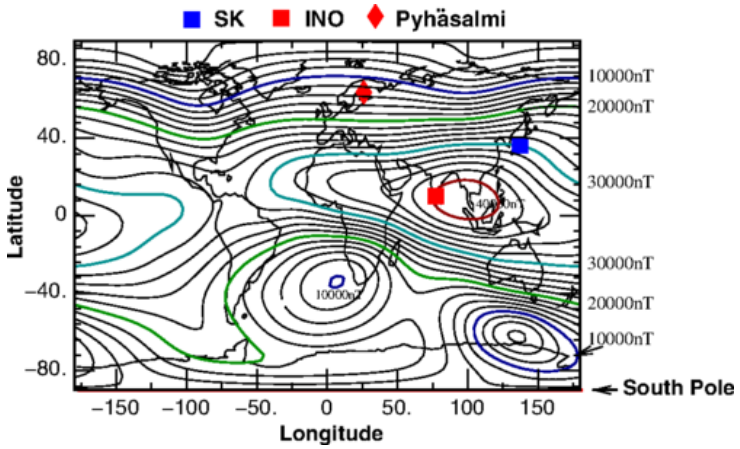

Figure 1.4: Horizontal component of the geomagnetic field, computed using the IGRF model for the year of 2010, together with some experimental sites. Figure from [34].

The FLUKA model

The FLUKA model [35] is a full 3D Monte Carlo (MC) package, which embeds the interaction model, particle transport and energy loss mechanisms. The Earth is assumed to be a sphere with a radius of 6378.14 km, while the atmosphere is parametrized as a medium composed by N, O and Ar, arranged in 100 concentric spherical shells. The geomagnetic cutoff is applied *a posteriori* on the final flux arriving to the detector, neglecting the particle bending. The hadronic interaction is simulated according to two separate models: up to 5 GeV, the *PEANUT* model is used, while a "color strings" approach is used at high energy. The flux is computed in the energy range $0.1\,\text{GeV} \lesssim E_\nu \lesssim 100\,\text{GeV}$ and is available online for a limited number of experimental sites (Kamioka, Gran Sasso and Soudan). The detector surface used in the simulation is larger than the actual detector and therefore the flux undergoes a final re-scaling, according to the true size.
The uncertainty on the atmospheric flux predictions are quoted at about $\pm 7\%$, even if they move from experimental measurements up to 10 - 20%.

The Bartol model

In the 3D Bartol model [36], primary particles are generated at fixed energy and then re-weighted at the end, to reproduce the observed spectra and at the same time benefit from statistics on the whole energy range. The solar wind effects, as well as the geomagnetic cutoff with the particle bending,

are considered. The Earth is assumed to be a perfect sphere, with a radius $R_E = 6372\,\mathrm{km}$ and primaries are generated on a spherical surface with radius $R = R_E + 80\,\mathrm{km}$. Particles are tracked up to a spherical surface of radius $R = R_E + 400\,\mathrm{km}$. Detectors are assumed to be larger than their real size, to achieve an increased statistics, and the flux is re-weighted at the end of the simulation to account for the actual size. The atmospheric neutrino flux is provided in the energy range $0.1\,\mathrm{GeV} \lesssim E_\nu \lesssim 10\,\mathrm{GeV}$ and is available online at the experimental sites of SNO, Soudan and Kamioka.

Chapter 2

Current status of atmospheric neutrino measurements

The atmospheric neutrino flux is a large experimentally available source, which has been widely used in the field of fundamental physics. Being spread over a wide energy range, it gives access to many sectors of particle physics. In relatively recent times (i.e. since 30 years) it has been also proved to be a powerful source for neutrino flavor oscillation studies, since the distance which occurs between the production and the detection sites can range from 10 up to 10000 km, making available a large window in the L/E space.
Past measurements include atmospheric neutrino studies with iron-based calorimeters (Fréjus [37], NUSEX [38]), water/ice Cherenkov detectors (IMB [39], Kamiokande [40], AMANDA [41,42]), time projection tracking calorimeters (Soudan [43]) and scintillator / streamer tubes detectors (MACRO [44]). Most of these experiments investigated the "ν_μ flux anomaly", who consists of a ν_μ flux reduction around the GeV because of the oscillation effects. Among these experiments, Fréjus and AMANDA have also provided a full measurement of the energy spectrum.
Present experiments who study the atmospheric neutrino flux are Super-Kamiokande [45], ANTARES [46] and IceCube [47–51], all based on the detection of Cherenkov light. In the sections below, experiments who have performed a measurement of the energy spectrum are described in more details. A basic distinction can be applied in terms of the detector size, whereas Fréjus and Super-Kamiokande investigated the lower energy sector of the spectrum and the largest ANTARES, AMANDA and IceCube the most energetic one.

2.1 Fréjus

The Fréjus experiment was located at the Fréjus underground laboratory, under the french-italian Alps, with a depth of 4.800 m.w.e. The detector consisted of a sandwich of flash chambers and iron planes, with Geiger tubes planes in the middle, for a total mass of around 900 tons. The sandwich cells were oriented vertically and horizontally alternatively, in order to provide two independent orthogonal view of the same event. A picture of the detector is in fig. 2.1 - left. The detector was able to track the deposited energy of each secondary particle after a neutrino interaction, as can be seen in fig. 2.1 - right. The energy resolution was about 10% at 1 GeV, decreasing at higher energy.

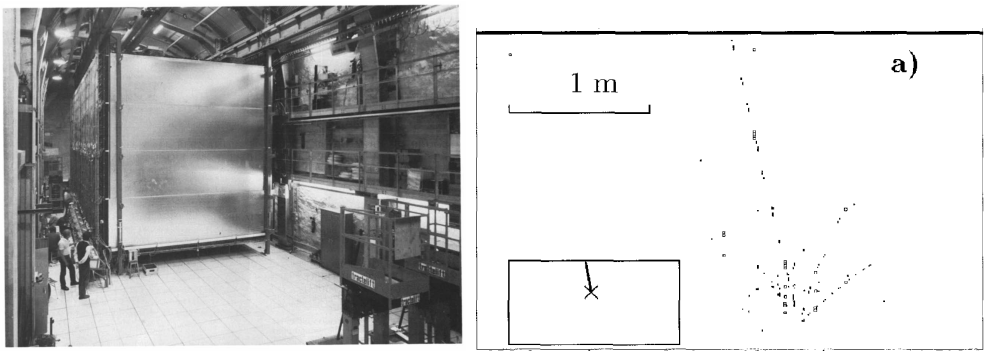

Figure 2.1: Left: picture of the Fréjus detector in the experimental hall; right: signature of a semi-contained ν_μ interaction in the fiducial volume. Figures from [52] and [37], respectively.

The detector was in operation from 1984 to 1988, in its final configuration from 1985 only. The atmospheric neutrino spectrum analysis relied both on events with neutrino interaction vertex inside the fiducial volume and outside. The second class includes upward-going stopping muons and horizontal through-going muons.
Events were selected or discarded upon a visual inspection and later subject to a pattern recognition program, to extract the visible energy. After all selections, the final data sample corresponded to an exposure of 2.0 kiloton-years. The final spectrum was unfolded on a MC-based technique and no significative deviation was found with respect to the predicted neutrino flux, thus rejecting the oscillation hypothesis. The final measured spectra are reported in fig. 2.2, in the range $320\,\mathrm{MeV} < E_\nu < 30\,\mathrm{GeV}$ for ν_e and in the range $250\,\mathrm{MeV} < E_\nu < 10\,\mathrm{TeV}$ for ν_μ.

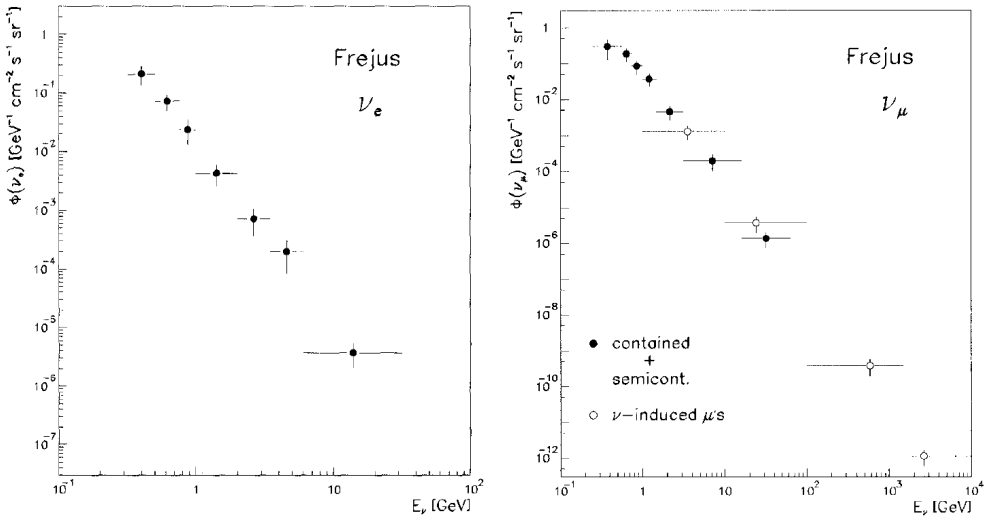

Figure 2.2: Reconstructed neutrino spectra from the Fréjus experiment. Left: ν_e; right: ν_μ. Figures from [37].

2.2 Super-Kamiokande

The Super-Kamioka Nucleon Decay Experiment [53] was, at the time of construction, the largest ever built water-Cherenkov detector. Originally, as for his predecessor Kamiokande, its primary goal was to investigate the proton decay. His design, however, makes it an excellent instrument for neutrino physics. The experiment definitely proved the existence of neutrino oscillations by analyzing the atmospheric neutrino flux [54].
The detector consists of a 50-kton volume, cylindrical-shape tank, filled with ultra-pure water. Relativistic charged particles which go through the water volume emit Cherenkov radiation, whose wavefronts are ring-shaped (fig 2.3). The tank is equipped with about 11.000 20" photomultiplier-tubes (PMTs), which detect the Cherenkov light. An outer water veto contains about 1.800 additional PMTs, to identify muons coming from cosmic rays.
The shape of the Cherenkov rings is highly sensitive to the type of particle that produced them, as can be seen from fig. 2.3. While muons proceed almost in straight line and generate well-defined contours, electrons are more subject to scattering and recoils, thus producing "fuzzy" edges on the rings. The differences in the shape of the rings are at the basis of particle identification, where the experiment achieved excellent performances. Furthermore, the Cherenkov radiation is directional and is strongly correlated with the particle direction, so that the initial neutrino direction can be inferred with

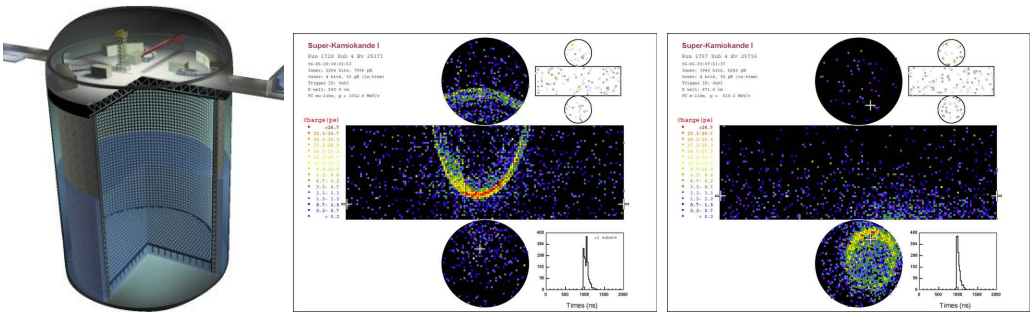

Figure 2.3: Left: sketch of the Super-Kamiokande detector; center: light pattern of a ν_μ CC event inside the water volume; right: light pattern of a ν_e CC event inside the water volume. Each dot represents a hit PMT. Credits: Super-Kamiokande Collaboration.

high precision by observing the secondaries.
Super-Kamiokande had five experimental phases from 1996, the last of which started in 2019. For this last one, named SK-V, a quantity of Gadolinium has been dissolved into the ultrapure water, to enhance the detector sensitivity to supernovae neutrinos.
In the atmospheric neutrino spectrum analysis [45], the events recorded by the detector are divided into several sub-classes, depending on the event topology (i.e. partially-contained, sub-GeV single-ring e-like...). The selections are targeted to identify CC ν_e and ν_μ events, which are used to estimate the total neutrino flux. As already mentioned, an high purity for each sample is achieved.
The final spectrum is obtained through unfolding techniques, first reconstructing the CC spectrum and then re-weighting bin-by-bin the total flux from the HKKM model [32, 33] with the measured CC spectrum. The spectrum obtained for ν_e and ν_μ flavors is reported in fig. 2.4. In the same work, the collaboration has also presented a measurement of the azimuthal distribution of atmospheric neutrino events (fig. 2.5), as well as an analysis of seasonal effects on the flux due to the solar activity. The angular-dependent analysis shows clearly the flux asimmetry effect introduced by the geomagnetic field.

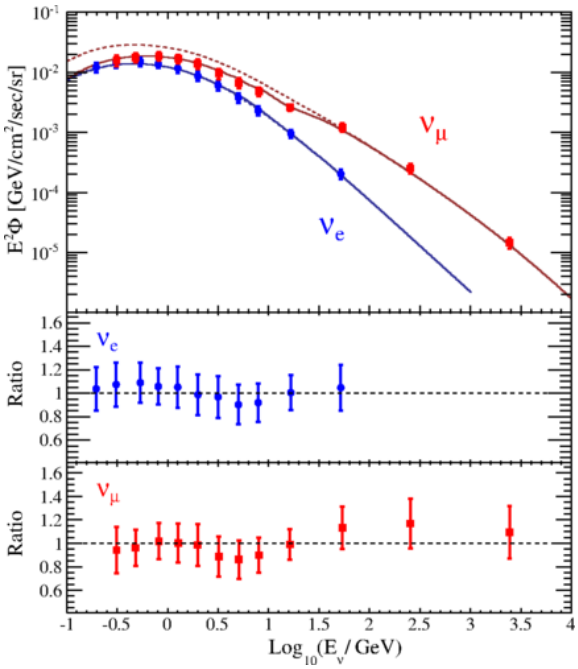

Figure 2.4: Atmospheric neutrino energy spectrum measured by Super-Kamiokande, for ν_e and ν_μ, compared with model predictions. The Data-model ratio is also reported. Figure from [45].

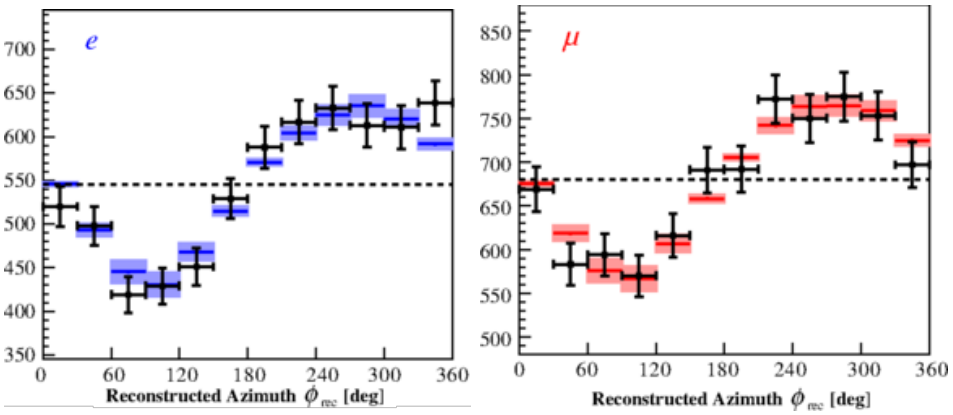

Figure 2.5: Reconstructed azimuthal distribution for e-like (left) and μ-like (right) events, together with MC predictions. Events are only considered for a reconstructed energy between 400 MeV and 3 GeV and with a reconstructed zenith angle θ_{rec} such as $|cos\theta_{rec}| < 0.6$. Figure from [45].

2.3 ANTARES

The ANTARES neutrino telescope [55] is a cherenkov-based detector and is located more than 2000 m underwater offshore from the southern french coast, in the Mediterranean sea. The construction ended in 2008 and it is in operation ever since. It consists of an array of 12 strings of 450 m each, with 60-75 m spacing in between. Each line is composed of 25 modules, each one hosting 3×10" PMTs facing downwards. The data collected by the PMTs are transferred on-shore by means of a 42 km-long electro-optical cable, which provides also the power supply. A sketch of the detector is in fig. 2.6, including a zoom on the optical modules. As for Super-Kamiokande, the optical

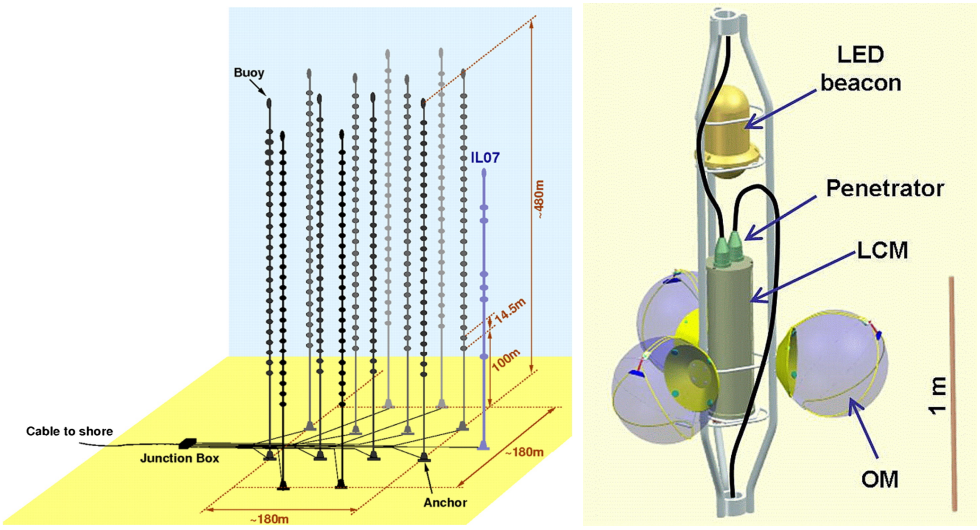

Figure 2.6: Left: sketch of the ANTARES detector; right: scheme of a storey, hosting three PMTs.

modules (OMs) detect the Cherenkov light produced by relativistic charged particles travelling into the water. The energy of particles is estimated from the amount of charge collected by OMs. The true neutrino energy spectrum has been extracted by means of two different unfolding methods, described in [46]. The measured ν_μ spectrum is reported in fig. 2.7 and is based on reconstructed muon tracks coming from below the horizon only, in order to increase the sample purity and reject the cosmic muon background.

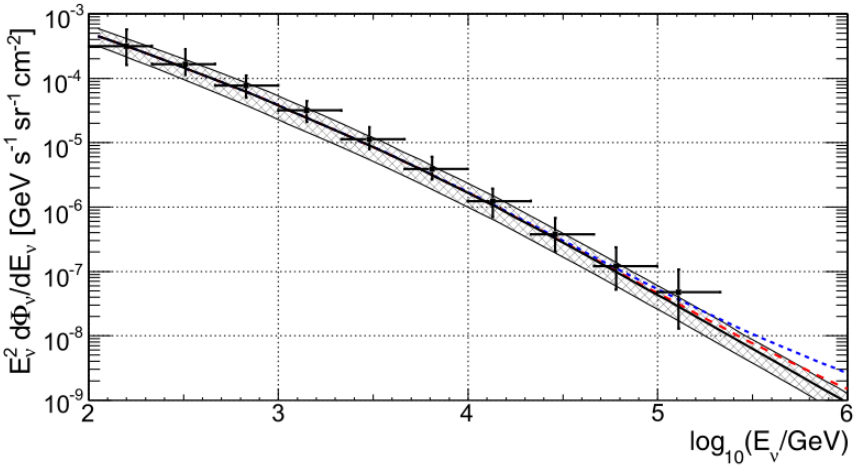

Figure 2.7: Atmospheric ν_μ energy spectrum measured by ANTARES. Figure from [46].

2.4 AMANDA and IceCube

The AMANDA neutrino telescope was in operation from 2000 to 2006 and employed the same detection technique of ANTARES: reconstruct the light pattern of Cherenkov radiation produced by relativistic particles. The only substantial difference is in the detector medium: AMANDA was located at the Geographical South Pole and was buried deep in the antarctic ice. The detector consisted of 677 8" PMTs facing downwards, arranged in 19 strings and placed at a depth of 1.5 km. The deep antarctic ice is extremely transparent ad allows the propagation of photons at great distances.
AMANDA data have been used to extract the atmospheric ν_μ energy spectrum, by means of two different methods: a forward-folding likelihood analysis [41] (fig. 2.8 - left) and an unfolding analysis [42] (fig. 2.8 - right).
The AMANDA detector was turned off on May 2009, when its successor IceCube was almost completed. The IceCube construction ended in 2010 and it is still in operation. The new detector features 86 strings in total, for an overall amount of 5160 digital optical modules (DOMs), placed between 1.5 and 2.5 km depth. Each DOM hosts a 10" PMT and is an independent DAQ unit. The total instrumented volume is around 1 km^3, so that the detector can access the highest energy region of the atmospheric neutrino spectrum. Furthermore, the impressive dimensions allowed the first observation of neutrinos from astrophysical sources [56]. 7 of the IceCube strings are placed in the core of the detector in a denser arrangement and form the *Deepcore*

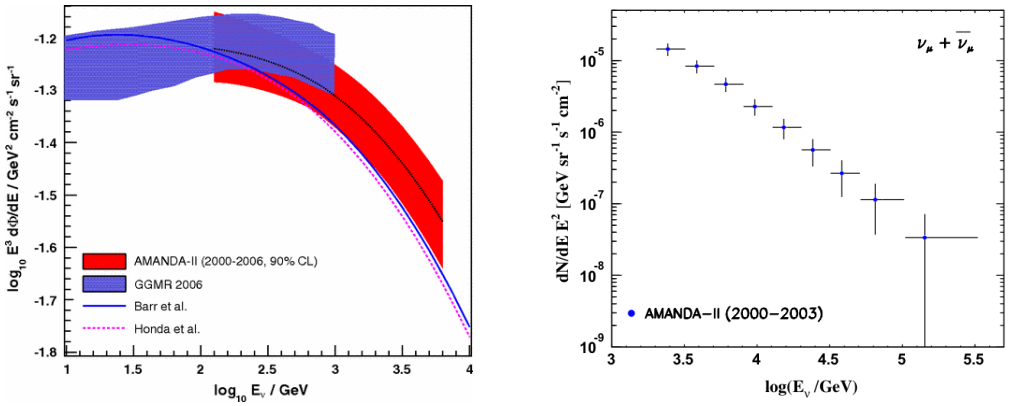

Figure 2.8: Left: atmospheric ν_μ energy spectrum as measured by AMANDA in [41]; right: ν_μ spectrum as measured by AMANDA in [42].

sub-detector. Deepcore is devoted to atmoshperic neutrino physics, including flavor oscillation studies, extending the energy range of the IceCube array down to $\sim$10 GeV. A sketch of the experiment, together with an example of an event-display, is in fig. 2.9.

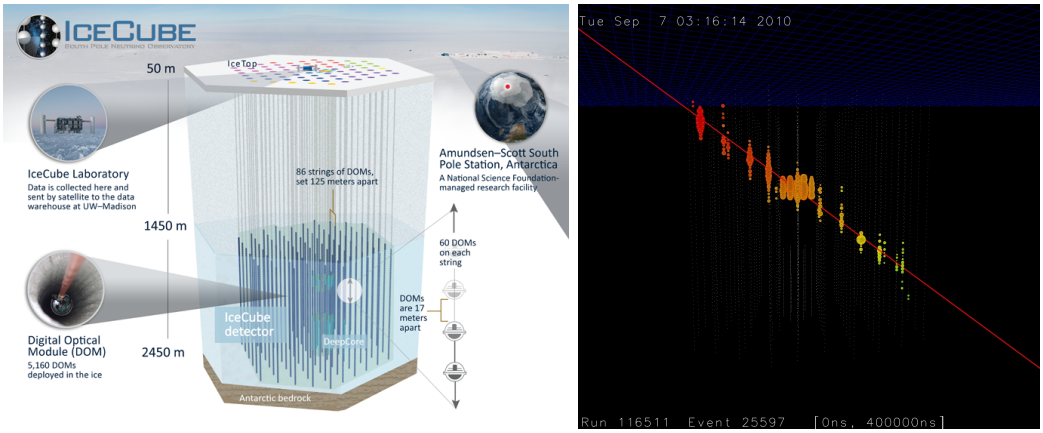

Figure 2.9: Left: sketch of the IceCube detector; right: example of a down-going muon in the IceCube event display. Each dot represents a hit PMT. The size of the dot is proportional to the charge collected. The red dots correspond to early hits, while yellow/green dots to late hits. The denser Deepcore array is visible in the middle. Credits: IceCube Collaboration.

The IceCube complex features also a surface detector, composed of 86 ice Cherenkov-based stations, used for Cosmic Ray physics and as an active

veto for the below neutrino detector [57].
The atmospheric neutrino flux has been obtained from various analyses in IceCube, covering an energy range from tenth of GeV up to the PeV region, both using the Deepcore sub-array [48] and the whole array [47,49–51]. Some recent results are in fig. 2.10.

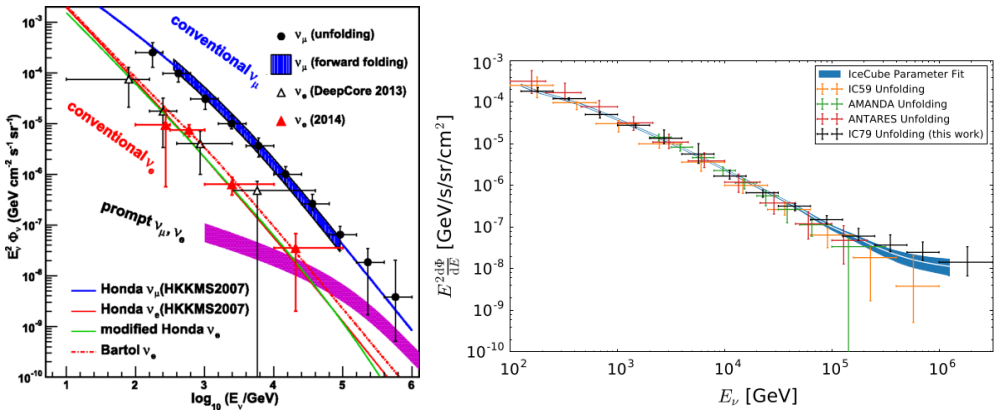

Figure 2.10: Left: IceCube atmospheric ν_e and ν_μ flux measurement comparison; right: ν_μ energy spectrum measured by IceCube, showing an excess in the PeV region, due to the astrophysical flux. Figures from [49] and [51], respectively.

Chapter 3

JUNO experiment

The Jiangmen Underground Neutrino Observatory (JUNO) is a multi-purpose neutrino experiment, proposed in 2008 to determine the neutrino mass hierarchy by detecting reactor antineutrinos [58]. The detector site has been chosen in order to achieve the best sensitivity to neutrino mass hierarchy. The JUNO complex is currently under construction in China, with a rock overburden above the experimental hall of around 700 m, and is located 53 km away from both Yangjiang and Taishan nuclear power plants. The total thermal power of the two reactor complexes, once completed, would be 35.73 GW_{th}. The symmetric distance from the two cores is necessary in order to avoid de-phasing effects in the detected antineutrino spectrum. The experiment is located in the Guangdong province, southern China, as depicted in fig. 3.1. The end of construction is scheduled for 2021.

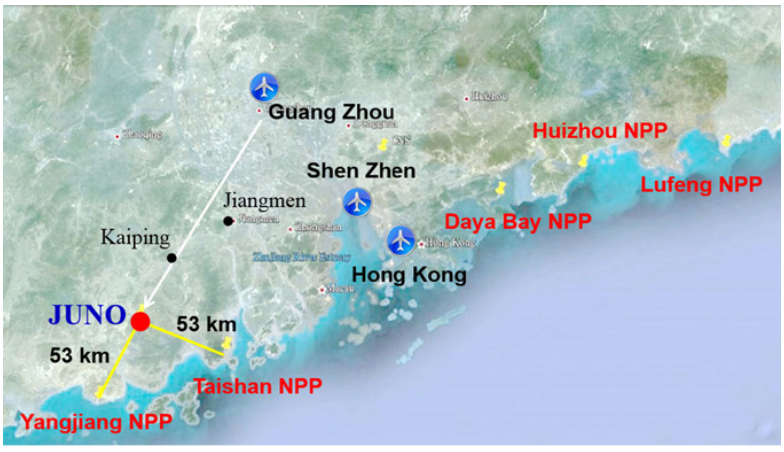

Figure 3.1: Location of the JUNO site, together with the main urban centres in the surroundings and the Daya Bay complex. Figure from [58].

The neutrino detector consists of a 20 kton fiducial mass liquid scintillator (LS), where antineutrinos produced in the nuclear power plants can interact via inverse beta-decays (IBD), producing a positron and a neutron in the final state: $\overline{\nu}_e + p \rightarrow e^+ + n$. The positron loses its kinetic energy in a short length and then annihilates with an electron: the sum of these two processes generates a *prompt* signal within few ns. The neutron is captured later with a typical delay of a few hundred μs and produces a *delayed* signal of 2.2 MeV.
The scintillation light from these secondary particles is collected by more than 40.000 photo-multiplier tubes (PMTs) installed on a spherical structure with radius $\simeq$ 20 m. PMTs are submerged in a buffer liquid to protect the LS from the radioactivity of the PMT glass. The scintillator liquid is composed of a mixture of several compounds, chosen in order to maximize the light production per neutrino event. The central scintillator detector is surrounded by a cylindrical water pool, design to detect the Cherenkov light from cosmic muons and to shield against the environmental radioactivity, acting as a veto detector. On top of the water pool there is another muon detector, made of scintillating strips, which has the role to accurately identify the muon tracks. A detailed description of the JUNO central detector, water pool veto and top tracker is given in Sec. 3.2.1, 3.2.2, and 3.2.3, respectively.
The design energy resolution is $3\%/\sqrt{E[MeV]}$ and will be addressed by maximizing the light yield (LY) and the PMT coverage. The JUNO final design includes 20" PMTs for the central detector and the water pool, to achieve the high photon statistics, plus 3" PMTs in the central detector to reduce systematics.
Given the planned resolution and the neutrino flux from the power plants, the mass hierarchy is expected to be determined in six years of data taking, with a confidence level between 3σ and 4σ. Beside the JUNO main goal, additional measurements are accessible to the detector. The reactor antineutrino flux can be exploited also for a measurement of the solar oscillation parameters $sin^2\theta_{12}$ and Δm^2_{21} with a sub-percent accuracy, which would represent the most precise measurement in the neutrino solar sector. Supernovae neutrinos can also be observed in case of a stellar explosion, inferring important information on the burst process at the source. The fine energy resolution can also be exploited to observe the solar neutrino flux, by means of elastic scattering on electrons. Another component potentially accessible to JUNO is constituted by geoneutrinos, produced by radioactive decays inside the Earth. Exotic searches include non-standard interactions, sterile neutrinos and dark matter annihilation signals.
Thanks to the detector large volume, several studies of the atmospheric neutrino flux can be also performed with competitive precision.

3.1 Scintillator detectors

Scintillation-based detectors represent a very widespread class of devices in use for experimental particle physics. The key feature is the emission of light (i.e. the *scintillation* process) as a result of an energy deposition by a passing particle. The energy loss excites the surrounding atoms and molecules, which then de-excite by emitting photons. The produced light is eventually collected by other devices coupled to the scintillators, like photomultipliers, which can convert the photon signal into an easy - readable electrical output. Large LSs had a great success in past years as neutrino detectors and for the search of rare processes. They are usually built underground, to be shielded from cosmic radiation, into an environment which is as most background-free as possible. LSs have the advantage of being easy scalable in dimensions and presenting a low threshold for the detection of neutrino events. Hence their wide use within the neutrino community.
LSs are composed of aromatic hydrocarbon structures which include the presence of benzene rings. Their common feature is a very rapid decay time ($\leq$ few ns or less). The emitted light typically peaks in the UV band and its time profile can be described with good approximation by a two - component exponential decay:

$$N(t) = A\ exp\left(\frac{-t}{\tau_f}\right) + B\ exp\left(\frac{-t}{\tau_s}\right), \tag{3.1}$$

where τ_f and τ_s are the two decay constants. Generally, one component is much faster than the other one, which is why they are referred to as, respectively, *fast* and *slow* component. Compared to other detectors, LSs are able to emit a huge quantity of light per deposited energy, which allows them to have a low threshold in detection energy. The light is usually collected by PMTs, which transform the light into an electrical output. Usual layouts include the installation of PMTs onto the detector inner surface, so that the cost scales with the surface area and large volume detectors can be constructed with reasonable costs. LSs share also other important features that make them suitable for large neutrino detectors: high light yield and attenuation length, good stability, compatibility with other detector materials, high flash point, low toxicity, appropriate density for mechanical stability and low cost [4]. On the other side, since the scintillation light has an isotropic spatial profile, the directional capability in the reconstruction of particle tracks is limited.

3.1.1 JUNO liquid scintillator

The core of the JUNO detector is formed by 20 kton of LS, contained inside an acrylic sphere of ∼36 m diameter. The LS is the target medium for the detection of neutrinos and antineutrinos. The main interaction channel for reactor $\bar{\nu}_e$ is the IBD on free protons, resulting in a prompt positron and a delayed signal from the neutron capture on hydrogen ($\tau \sim 200\,\mu$s). [59]
The JUNO LS is composed of several materials: the solvent liquid is Linear alkylbenzene (LAB) and forms the bulk of the target material. The dopant is a two-component system of the flour 2,5-Diphenyloxazole (PPO) and the wavelength-shifter 1,4-Bis(2-methylstyryl)benzene (Bis-MSB) , that are added at low concentration (2.5 g/l and 3 mg/l, respectively). The resulting shifts increase the wavelength of the emitted photons to $\sim$ 430 nm. The output longer wavelength avoids spectral self-absorption by the solvent and allows a high fraction of the photons to reach the PMTs. Compared to other materials, the scintillation process is very efficient: about 10^4 photons are emitted per MeV of deposited energy.
The target energy resolution of JUNO is 3 % at 1 MeV, corresponding to at least 1100 photoelectrons (PE) per MeV of deposited energy, considering photo-statistics only. Compared to the Borexino experiment, it corresponds to more than twice the PE yield in a detector 200 times the mass. To meet this demanding requirement, both the initial LY and the transparency of the liquid have to be optimized simultaneously. During all the preparation time before the JUNO start, a broad spectrum of laboratory measurements have been performed and are ongoing, in order to characterize different brands of LAB and wavelength shifters. A close contact with the producing companies has been established and allows the optimization of the production quality within certain limits [59]. Low background conditions are achieved through a series of purification processes in situ [60]. The contamination level requirements are reported in table 3.1, divided for the two physics target in the low energy region: reactor $\overline{\nu}_e$ and solar ν_e.

Channel	^{238}U	^{232}Th	^{40}K
Reactor $\overline{\nu}_e$	$\leq 10^{-15}$ g/g	$\leq 10^{-15}$ g/g	$\leq 10^{-16}$ g/g
Solar ν_e	$\leq 10^{-17}$ g/g	$\leq 10^{-17}$ g/g	$\leq 10^{-18}$ g/g

Table 3.1: Contamination requirements for reactor and solar neutrino analysis. The specification for the three main contaminants are reported. Values from [59].

Moreover, a large-scale test is being conducted in one of the Antineutrino

Detectors of the Daya-Bay experiment, which will allow to study the effect of purification on a sample of about 20 tons of LS.
The final designed performances include a LY $\sim 10^4$ photons/MeV and an attenuation length $\geq 20\,\text{m}$ at 430 nm.

3.2 JUNO detector design

The JUNO detector consists of a central detector, which is the primary target for neutrino interactions, plus a veto system: a cylindrical water pool which surrounds the central detector and a muon tracker on top of it. A schematic view is reported in fig. 3.2. The detector design has been optimized in

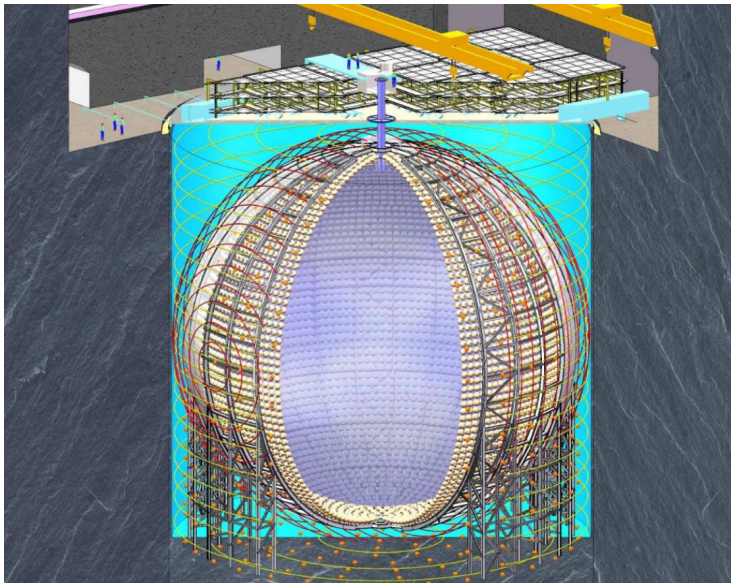

Figure 3.2: Schematic view of the JUNO detector complex. The central spherical detector is surrounded by a cylindrical water pool and both are below the top muon tracker.

order to achieve an high statistics of IBD from the nearby reactors and reject both the external and internal background with high efficiency. To meet the planned energy resolution, a series of minimum requirements have been established [58]:

- a PMT coverage for the central detector $\geq 75\%$;
- a PMT photocathode quantum efficiency $\geq 35\%$;

- a LS absorption length $\geq$ 60 m, corresponding to an attenuation length $\geq$ 20 m at 430 nm (see previous section).

In order to fulfill all the technical goals, dedicated working groups have been established for each of the subsystems: water system, acrylic panels, PMT instrumentation, etc. At present time, all activities are in the final stage, with contacts with external companies and first deliveries of the material. Tests on all the instrumentation are ongoing, with the aim of keeping all the technical aspects strictly under control.

3.2.1 Central Detector

Once completed, the JUNO central detector (CD) will be the largest ever instrumented volume filled with LS. The technical challenges are many and require a careful control of all the aspects.
The CD primary target is to measure the reactor $\overline{\nu}_e$ spectrum with an energy resolution equal to $3\%/\sqrt{(E[MeV])}$. The final design includes a 20 kt LS volume, contained inside an acrylic sphere. The scintillation light from the LS is collected by $>$ 17.000 x 20" PMTs ("large" - LPMTs) and $>$ 25.000 x 3" PMTs ("small" - SPMTs), installed on a larger stainless steel (SS) spherical structure (fig. 3.3). An important point to consider is that the CD must mantain a low background level from natural radioactivity. The radiopurity of all components, included the LS, is indeed of primary importance in the choice of the materials for the construction and of the manufacturer companies. A number of radioactivity tests are hence performed, regarding the acrylic panels, the PMTs, the truss, etc.
A final fundamental requirement concerns the long - term stability of the detector. The structure has been designed in order to avoid leakages among different sections and to mantain its robustness throughout a 20-years period [59]. The project includes also a relatively short construction time ($\sim$1.5 years) and an affordable cost.
The inner acrylic sphere has a thickness of $\sim$12 cm and an inner diameter of 35.4 m. The inner diameter of the SS truss is $\sim$40 m , supported by a number of columns which are built on the base of the water pool (fig. 3.3). For the acrylic sphere, a chimney with an inner diameter of $\sim$1 m is placed at the top of the sphere, serving as door for the LS filling and as interface for the calibration system. The relative pressure between the LS and the water has a non-negligible effect on the acrylic sphere. The chimney is designed to be a few meters higher than the water level, in order to provide flexibility in setting the LS relative height and the resulting stress in the sphere. Due to the height of the chimney above the sphere, an optical isolation is foreseen to

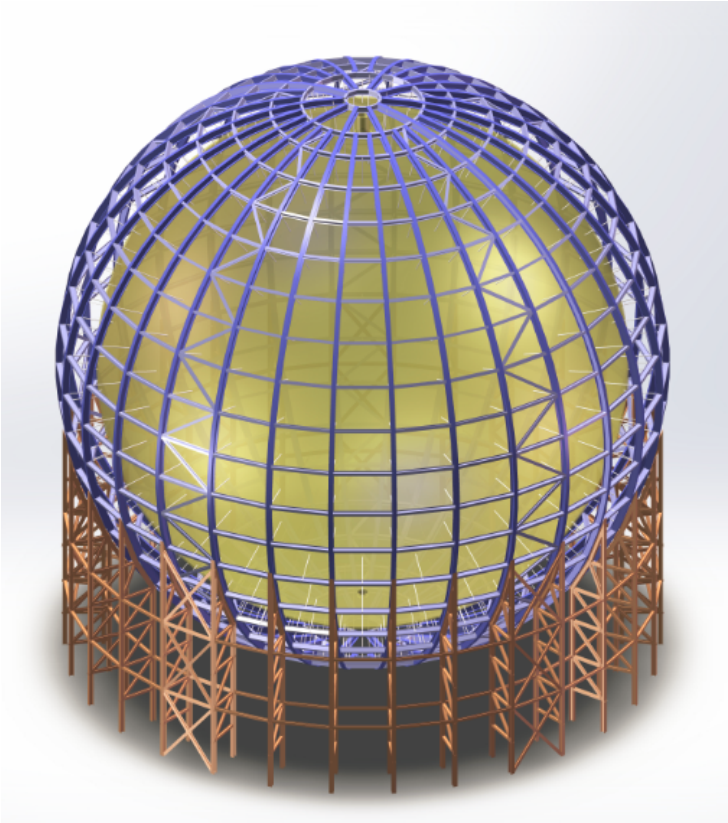

Figure 3.3: JUNO central detector. The SS truss is visible, togeteher with the supporting pillars. The truss supports the inner acrylic ball by means of acrylic rods. PMTs are not displayed.

block the background-induced light from being detected by the PMTs. The ∼40.000 (LPMTs + SPMTs) inward-facing PMTs are arranged directly on the SS truss and are submerged in a ∼2 m-thick water buffer which shields the LS from their radioactivity. An opaque layer optically separates the central detector from the outer water veto detector.

SS structure

The SS structure is a spherical, single-layer truss made of I-shaped components, arranged in both longitudinal and latitudinal directions. The truss is supported by pillars at the base of the water pool. In order to avoid torsions of the structure, a ring of spiral bracings are added in the truss grids. Finally, due to space limitation in the pole region of the truss, the square

shaped structure is replaced by a triangle shaped one, so that number of truss members is reduced.

Acrylic sphere

The acrylic sphere is assembled by means of polymerization techniques in a series of acrylic sheets. Taking into the accounts the limits from production and transportation, the sphere is divided into more then 170 sheets (fig. 3.4), each one with a surface $\sim$ 3 x 8 m^2. A top chimney is included in the final design. An outlet is also foreseen at the bottom of the sphere, for acrylic cleaning and LS recycling during detector running. To support the acrylic

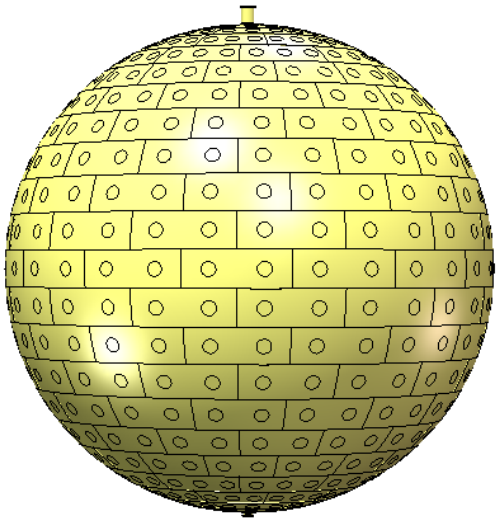

Figure 3.4: Schematic view of the acrylic sphere.

sphere, each acrylic sheet hosts one or two stainless steel disks, which are embedded in it as a connecting structure (fig. 3.5). The steel disk is designed to have a ball-type head, and a supporting rod connects it to the truss. The load on the acrylic sphere is therefore transferred to the truss through the rods.

Central Detector Calibration System

In addressing the whole series of precise measurement, the JUNO detector (and in particular the CD) needs to take into account all the systematics that come from the photon yield fluctuations and the detector non-uniformities. A very careful determination of these systematic effect at sub-percent level

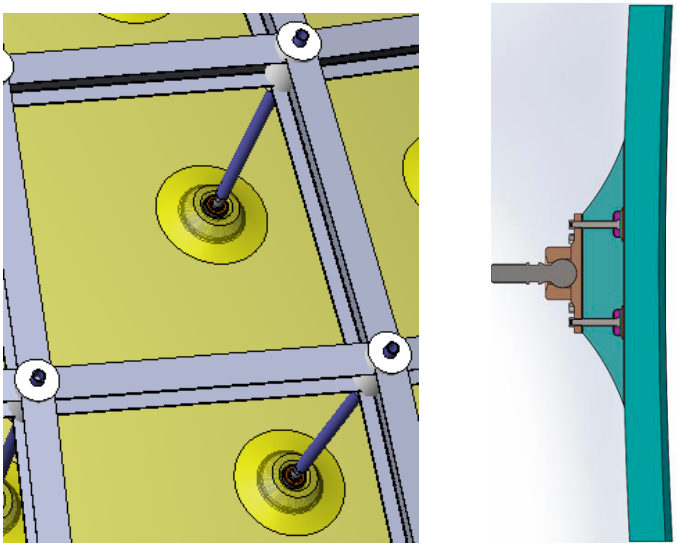

Figure 3.5: Detailed view of the connecting rods between the acrylic sphere and the SS truss. Left: overall view of the system; right: detail of the interface at the acrylic surface.

is of primary importance for JUNO. The detector design includes therefore varoius calibration systems, to be operated in situ during different campaigns. The designed systems are the following [61]:

ACU: Automatic Calibration Unit, it consists of a rope system, which is able to move along the vertical axis. The ACU supports the usage of different calibration sources, like γ, neutron and laser, with a positioning precision of few mm. The ACU calibrations are planned to be performed weekly.

CLS: Cable Loop System, consists of a 2-cable loops system, which allows a full scan on a 2D plane. The source position is controlled by spools, with an accuracy on the position $< 10\,\text{cm}$. The CLS system is planned for a monthly calibration.

GTCS: Guide Tube Calibration System, designed to scan the surface around the acrylic sphere, so to provide boundary conditions for the calibration map. The accuracy on the position is $< 10\,\text{cm}$, with a monthly planned campaign.

ROV: Remotely Operated Vehicle, which consists of a self-driven vehicle ($0.7\,\text{m} \times 0.3\,\text{m}$) for a full 3D scan of the LS volume. The position accu-

racy is planned to be around 4 cm, ensured by means of an ultrasonic emitter. The ROV calibration is planned to be performed annually.

The target for the calibration system is to keep the non-linearity effects in the energy reconstruction below 1%.

3.2.2 Water Pool

Given the extremely precise measurements that JUNO is going to address, the background control is again fundamental. The cosmic muon background, in particular, is a very prominent source of background events, in several ways:

- prompt light from muon ionization;
- ^{9}Li and ^{8}He background from muon spallation and muon shower particles;
- fast neutron background from muon induced high energy neutrons.

The muon-induced background is of the order of several Hz in the CD and has to be compared with the ∼60 events/day from reactors IBD and even less event rates for other neutrino sources. An high efficiency muon veto system, designed to identify those events, is therefore necessary.
The JUNO Water Pool (WP) is a water Cherenkov detector designed to identify cosmic muons with high efficiency. It consists of cylindrical tank, filled by ∼20 kt of ultrapure water (fig. 3.2), which surrounds the CD. The WP cylinder has a 43.5 m diameter and is 44 m tall. The Cherenkov light produced in the water is collected by 2400 LPMTs, arranged on the windows of the spherical SS frame and facing outward (fig. 3.6). Both the walls of the pool and the external surface of the sphere are covered with high - reflectivity (around 92%) Tyvek film to increase the photon collection. The WP veto is designed to achieve $> 95\%$ efficiency in tagging cosmic muons. A series of LED are placed at different positions in the WP for calibration purposes [59].

3.2.3 Top Tracker

In order to improve the reconstruction of cosmic muons direction, a plastic scintillator strips tracker is placed at the top of the WP. A 3-layers design has been adopted (fig. 3.7). The scintillator layers are reused from the decommissioning of the OPERA target tracker [63]. The detector is composed of 63 walls with a sensitive area of 6.7 x 6.7 m^2 each. A target tracker module is composed of 64 scintillating strips, 6.7 m long and 26.4 mm wide. Each

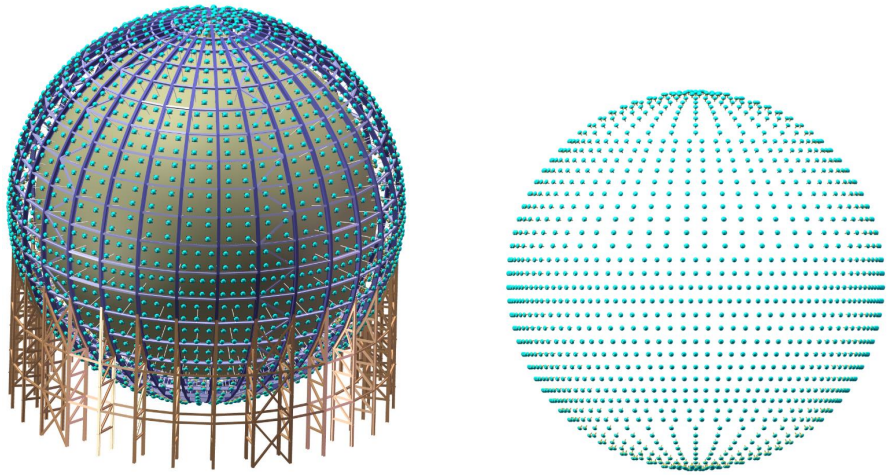

Figure 3.6: Scheme of the WP LPMTs arrangement on the SS truss (left) and alone (right). The PMTs are denser in the lower part of the detector, after optimization studies within the collaboration. Figures from [62].

strip is read out on both sides by a Hamamatsu 64-channel multi-anode PMT (fig. 3.8). The walls are arranged in a 7 x 3 grid scheme. Furthermore, since

Figure 3.7: 3-layer structure of the TT, together with the supporting structure. At the chimney position, 3 scintillator layers are placed, above the TT level. Figure from [62].

radioactivity from the surrounding rock of the experimental hall can induce extremely high noise rate in the plastic scintillator strips, the 3-layers design reduces this contribution by means of a coincidence logic. The distance between two layers is 1.5 m, which is reduced for the section above the chimney. The top tracker (TT) can cover ∼25% of the area of the top surface of the WP.
The TT strips have been produced by extrusion, with a TiO_2 co-extruded

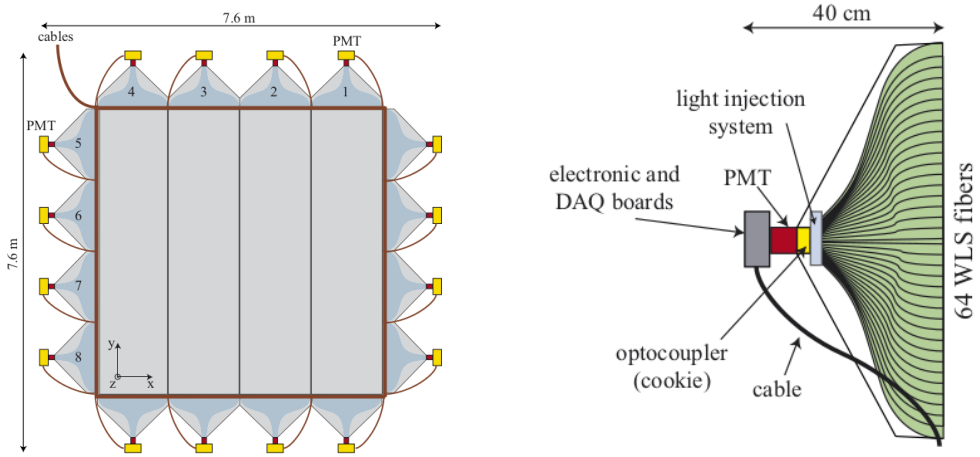

Figure 3.8: Scheme of the TT detector components. Left: schematic view of one wall; right: schematic view of the endcap of a scintillator strip module. Figures from [63].

reflective and diffusive coating for better light collection [59]. A long groove running on the whole length and at the center of the scintillating strips houses a wavelength shifting fiber, which is glued inside the groove using a high-transparency glue. This technology has proved to be very reliable, due to the robustness of its components. Delicate elements, like electronics and PMTs, are located outside the sensitive area, where they are easily accessible. The OPERA target tracker was originally placed in vertical position [63], while in the case of JUNO the TT layers are arranged horizontally. This difference implied a re-design of the supporting mechanical structure, which consists of a ∼500 tons, 48 x 25 m^2 carbon steel truss [62]. This bridge hosts also the calibration room of the CD and the water and scintillator pipes.
Given its limited coverage of the solid angle atop the CD, the TT is not intended to serve as an active veto for JUNO. Indeed, its goal is to provide a sample of well-identified cosmic muons, to be used for the calibration of WP and CD performances in reconstructing such events.

3.3 JUNO PMTs

The light produced by the LS is converted into an electrical signal by means of PMTs. In order to accomplish the JUNO physics goals, the PMTs requirements include high photon detection efficiency (PDE), large area, low cost, low noise, high gain, high stability and long lifetime. The first design

included LPMTs only, while in the current scheme a double system of > 17.000 LPMTs and > 25.000 SPMTs are arranged on the CD. The final photocathode coverage is > 78%.
The LPMT system has been designed in order to maximize the photon collection and therefore obtain a high energy resolution. The SPMT system is indeed designed to increase the detector performances at high energy and reduce detector systematics, since they operate in single-photon counting regime within a wide energy range.
The PMT system is designed to mantain full functionality for more than 20 years.

20" PMT system

The specifications of the LPMT system include the state-of-art of current large PMT technology, such as a peak quantum efficiency $\geq 38\%$ at 420 nm and a total PDE $\geq 35\%$. The full list is reported at pag. 139 of [59]. The demand of a large area PMT with a quantum efficiency (QE) above 30% and with a dynamic range spanning 3 - 4 orders of magnitude required a dedicated R&D, since no device with such features was on the market at the beginning. The efforts have led to a collaboration between IHEP Beijing and the chinese NNVT company, resulting in the development of a 20" Micro-Channel Plate (MCP) PMT with the required performances (fig. 3.9 - left). 15.000 of these MCP PMTs are being produced by NNVT for JUNO, to be used both for the CD and for the WP. Their Time-Transit Spread (TTS), however, is greater than 10 ns, which is not a negligible value. In the same years, the japanese company Hammamatsu developed a commercial 20" dynode-PMT with high performances in terms of PDE, designed mainly for the future Hyper-Kamiokande detector (fig. 3.9 - right). The advantage is the low TTS of such PMTs, around 3 ns. A contract has been signed between the JUNO collaboration and Hammamatsu, which already concluded the production of 5.000 PMTs for JUNO. These PMTs are used in the CD only. Thanks to the very good timing performances, Hammamatsu PMTs can improve the resolution in the vertex reconstruction. Delivered LPMTs are currently under testing in a dedicated facility and performances of a first batch are given in table 3.2.

3" PMT system

The high coverage of the LPMT system allows to detect a large number of PEs for neutrino events, with a yield estimated at ∼1200 PEs/MeV. For events close to the CD edge, however, a large fraction of the charge is col-

PMT type	Res. [%]	τ_{Rise} [ns]	τ_{Fall} [ns]	DCR [kHz]	PDE [%]
NNVT	32.95	4.54	15.85	42.51	27.45
Hammamatsu	27.67	6.70	10.21	19.10	28.49

Table 3.2: Summary of measured 20" PMTs performances on a first batch. The values are reported separately for NNVT and Hammamatsu PMTs. "Res." represents the charge resolution for single photo-electron (SPE) detection; "τ_{Rise}" and "τ_{Fall}" refer to the rise and fall time of the SPE waveform; "DCR " stays for dark current rate. Values from [64].

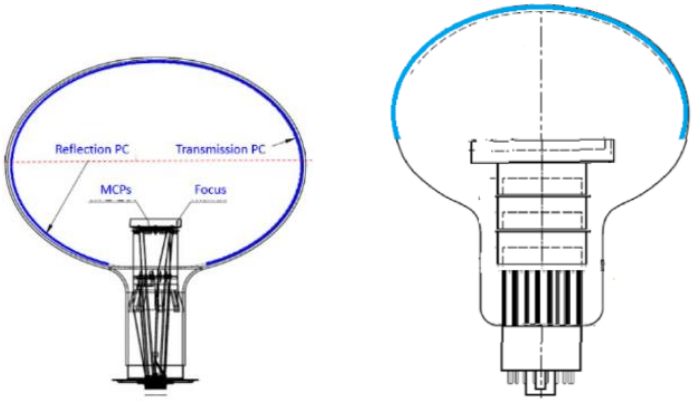

Figure 3.9: Scheme of the two types of LPMTs used in JUNO. Left: NNVT MCP-PMT; right: Hammamatsu dynode-PMT. Figures from [65].

lected by few PMTs, which can undergo saturation in their acquisition. Even if the dynamic range of LPMTs is wide, the systematic errors associated with the charge integration, such as the non-linearity, can be important.
To reduce this contribution, a system of 3" PMTs has been designed. The SPMTs are placed in the spaces between the LPMTs and distributed uniformly on the sphere. Given the small photo coverage, of the order of 3%, the SPMT system operates in photon-counting mode in the region of interest for reactor IBD events. The primary goal is to provide additional information with reduced systematics, looking at the same events of LPMTs.
Another important contribution of the SPMTs is the reconstruction of high-energy events, such as cosmic muons. Their effect is to extend the dynamic range of the detector, where the non-linearity effects on the LPMTs become important. They also improve muon tracking through their better timing, which is of particular relevance for keeping the backgrounds produced by cosmic-ray muons under control. Moreover, not being saturated even by

high deposited energy, they provide more ability to distinguish muon bundles. Further advantages come from the smaller pile-up they have, with respect to LPMTs, in case of high rate events, such as supernovae explosions. They can also perform independent measurements of solar oscillation parameters from reactor neutrino events, to serve as a cross-check for the LPMT system [66].
All the JUNO SPMTs are produced by the chinese company HZC and tested at the production site. Table 3.3 summarizes some measured performances of a first small batch of SPMTs.

Res. [%]	DCR [kHz]	QE [%]	TTS* [ns]
32.95	0.49	24.77	4.95

Table 3.3: Summary of measured 3" PMT performances on a first batch (3000 pcs). "Res." represents the charge resolution for single photo-electron detection. Values from [67].
*the TTS measurement is performed on a 91 SPMTs subsample only.

An aspect to take into account in the detector design is also the geomagnetic field effect on the PMTs performances. At the JUNO location, the total contribution is around 45 μT. The effect on LPMTs, which have a large photon collection area, can be very large, up to a 70% collection efficiency decrease [59]. In order to compensate the geomagnetic field effect, current-flowing coils are wrapped around the central SS sphere. After the compensation, the geomagnetic field impact becomes negligible. Further details can be found in [68].
Another aspect to take into account in the construction of a large liquid material-based detector is the PMT protection from shock waves. The water pressure on a PMT glass could indeed cause the implosion of the PMT itself. The problem comes from the fact that the subsequent shock wave can propagate through the liquid material and generate a cascade effect on the other PMTs. An example is given by the Super-Kamiokande accident in 2001 [69]. In order to protect PMTs from an implosion chain reaction, an acrylic shell for the upper half sphere, plus a SS coverage for the lower part, are designed. Tests on the materials are undergoing, to optimize the final design. Further details are in [70].

3.4 DAQ and trigger strategy

The JUNO readout system has to deal with the acquisition of signals from more than 20.000 LPMTs (CD + WP) plus 25.000 SPMTs. The amount of collected PEs spans from the few hundreds at < 1 MeV events to the millions of atmospheric events. The events have to be recorded over the whole range, ensuring the minimum data loss. The trigger system plays the crucial role of pre-selecting interesting events from the vast amount of random dark noise pulses recorded by PMTs. The electronics system must therefore ensure an excellent resolution over energy and time, with a negligible deadtime for high rate events (i.e. Supernovae explosions).
Concerning the CD, the electronics system is designed to provide a full LPMTs waveform digitization, by means of a high speed (1 Gsample/s), high resolution (12 bits) ADC. At the same time, it provides the sampling over the full dynamic range, from 1 up to about 4000 NPEs. The SPMT system, on the other way, does not need a full waveform acquisition, since it operates primarily in photon-counting mode. Both the LPMT and SPMT front-end electronics are placed underwater, into dedicated boxes. Each box includes one Global Control Unit (GCU). For LPMTs, one box acquires 3 PMTs (design valid also for the WP), while for SPMTs one box acquires 128 SPMTs. The output of the GCU is transferred out of water via an asynchronous link to the DAQ system and via a synchronous link to the trigger system, where the information of all LPMTs are combined to form a global trigger decision. The final trigger scheme is still under optimization. An acquisition time window of 1.2 μs is foreseen. More details on the LPMT electronics are at [71].
At the current stage, a trigger driven by a majority logic of LPMTs in the CD is foreseen: if > 350 fired PMTs in a 300 ns time window are found, the event is recorded in a 1.2 μs window. 350 PMTs roughly correspond to 350 keV of deposited energy.
A global trigger scheme is currently under construction, with the final goal of merging the information of the whole LPMT system. SPMTs and the TT feature an independent acquisition system. The TT DAQ, in particular, is devoted to trigger on cosmic muon events. As explained in sec. 3.2.3, these events are used for calibration purposes. The information coming from the TT sub-detector are therefore not used in this thesis.
According to the time and NPE pattern, a fast reconstruction of the event is performed online, regarding the estimation of the deposited energy and the interaction vertex. The events are therefore classified online, so to perform a higher-lever selection on the event flow. The raw data are then stored locally in a dedicated farm and then transferred to the IHEP Beijing Computing Centre. The JUNO computing model includes a full mirroring of raw data with some European sites.

Chapter 4

Monte Carlo simulation

All the performances of a future detector are nowadays evaluated by means of Monte Carlo (MC) simulations. Through these programs, it is possible to generate the full chain of interactions and the detector responses to a particular signal. In the case of neutrino events, simulation of interactions with electrons, nucleons and nuclei are available. Once an initial neutrino flux is assumed, a neutrino MC generator takes an input neutrino + target and produce a set of 4-vectors for particles emerging from the interaction [4].
These generators are able not only to simulate the initial neutrino interaction, but also re-interactions of secondary particles within the nuclei and therefore embed a great variety of particle and nuclear processes. Cross section libraries are therefore included for all the relevant processes.
Today, MC generators are an extremely powerful tool for data analysis. They constitute the link between the experimental reconstructed quantities and the true quantities and are necessary to make predictions about performances of future experiments. They are widely used by the scientific community, from the detector design stage through the extraction of physics measurements from reconstructed observables. MC neutrino generators play unique and important roles in the experimental study of neutrino interactions and oscillations and are constantly improved by new experimental results.
Since JUNO is still in the construction phase, all physics studies rely on MC simulations only. In order to get an output set of simulated physical observables, the simulation chain proceeds in three main steps:

- input neutrino flux assumption;
- neutrino interaction inside JUNO volume and production of secondary particles;
- propagation of secondary particles, photon emission and interaction

with the photo-cathode.

The MC simulation used in this work includes a total amount of 500.000 neutrino interactions, corresponding roughly to 400 years of detector live-time. The primary neutrino flavors considered are ν_μ, $\overline{\nu}_\mu$, ν_e and $\overline{\nu}_e$. The events have been generated with a primary neutrino energy up to 20 GeV.

4.1 Simulation of the atmospheric neutrino flux

As already discussed in Sec. 1.3.1, to reproduce the atmospheric neutrino flux observed, several models are available. In this work, the HKKM14 model [34] has been used to parametrize the neutrino flux. The model provides the neutrino flux prediction, in terms of energy and arrival direction, in the energy range [100 MeV - 10 TeV]. The flux is calculated separately for ν_μ, $\overline{\nu}_\mu$, ν_e and $\overline{\nu}_e$ and is available online. The energy distribution of the neutrino flux at the JUNO location, separated for each flavor, is reported in fig. 4.1.

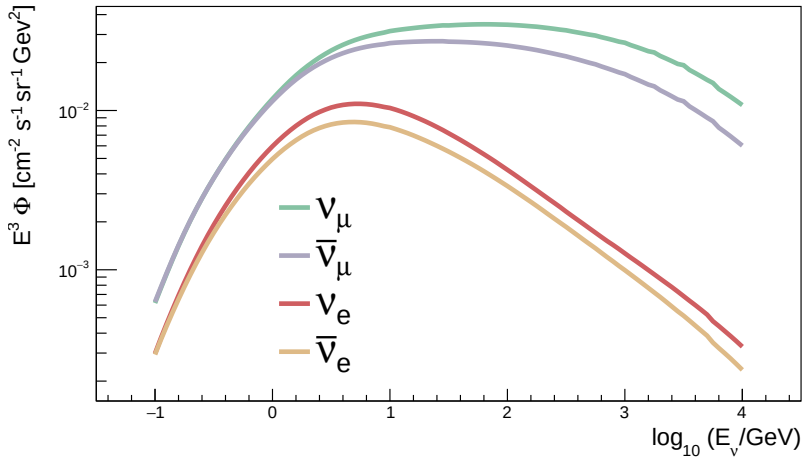

Figure 4.1: Atmospheric neutrino flux at the JUNO location, according to the HKKM14 model [34]. The flux is displayed separately for each neutrino flavor and is multiplied by the cube of the energy, for a clearer separation.

In the HKKM parametrization, the neutrino flux is calculated at the source, therefore no oscillation effect is included. In order to get a realistic prediction of the flux at the JUNO detector site, neutrino oscillations has been applied to the original flux, including matter effects. The flux modification depends

on the baseline and on the energy, as explained in Sec. 1.2. The oscillation parameters adopted are those reported in table 1.1, assuming normal ordering. The value of $sin^2\theta_{23}$ makes an exception, since it has been set to 0.5.

4.2 Neutrino interaction

Neutrino interactions are generated through the GENIE neutrino Monte Carlo generator [72], assuming the energy spectrum and arrival direction distribution as in the HKKM14 model. GENIE is a ROOT-based [73], object-oriented C++, open source software, developed with the final aim to simulate neutrino interactions from the MeV to the PeV energy scale. In the current version, the software is able to simulate events from 100 MeV to hundreds of GeV. The main efforts have been concentrated in the few-GeV energy range, which is the non-trivial transition region between non-perturbative and perturbative regimes.
From the first release in 2007, GENIE has updated its libraries according to the recent experimental results, mainly from neutrino beamline experiments, such as MINOS [74], Minerva [75], T2K [76] and NOvA [77]. The GENIE project is supported by a group of physicists from all major neutrino experiments operating in this energy range and therefore constitutes a wide and inclusive high-energy physics collaboration.
Neutrinos undergo in general a great variety of interactions. The relative weight of each interaction channel depends mainly on the energy of the incoming neutrino and their precise calculation is fundamental to estimate the final topology of the events. Furthermore, the particles produced after a neutrino-nucleon interaction can re-interact within the nucleus itself. This series of secondary processes are known as final state interactions (FSI) and their modeling involves many aspects of nuclear physics and strong interactions. In general, FSI treatment is one of the largest differences among models of the neutrino-nucleus interaction.
All processes in GENIE employ the relativistic Fermi gas (RFG) nuclear model, implemented through a modified version of Bodek and Ritchie [78]. The scattering kinematics for nucleons in a nuclear environment are in general different from those obtained in scattering from free nucleons. In the case of quasi-elastic and elastic scattering, GENIE applies Pauli blocking. For nuclear targets a nuclear modification factor is also included, in order to account for observed differences between nuclear and free nucleon structure

functions which include shadowing, anti-shadowing, and the EMC[1] effect [80]. GENIE incorporates a variety of cross-section models, which provide a calculation of the differential and total cross-sections. The total cross-section is used together with the flux to determine the rate of interacting neutrinos. Cross-sections for specific processes are then used to determine the relative weight of the interaction channels, while the differential distributions for that interaction model are used to determine the event kinematics. The composition of the target (i.e. the mass fraction of each isotope which forms the target) is given as an input to the generator.
The primary interaction processes included in GENIE are listed in table 4.1 and are further described below.

Interaction channel	Process
quasi-elastic scattering	$\nu + N \to \ell + N'$
elastic scattering	$\nu + N \to \nu + N$
baryon resonance production	$\nu + N \to A \to N' + m/\gamma$
coherent neutrino-nucleus scattering	$\nu + \mathcal{N} \to \nu/\ell + \pi + \mathcal{N}$
deep inelastic scattering	$\nu + N \to \nu/\ell + X$
neutrino-electron elastic scattering	$\nu + e \to \nu + e$

Table 4.1: Neutrino interaction channels implemented in GENIE. N and N' are the initial and final nucleon state (p or n). $\mathcal{N}$ is a generic nucleus state. X is a generic final hadronic state. ℓ is a generic lepton (e, μ, τ). A is a generic baryonic resonance state. m is a generic meson (π, η, ...). Here, the specific interaction channels involving charm mesons have been neglected.

Quasi-elastic scattering (QE) is the dominant process below $\sim$1 GeV, where a neutrino undergoes a CC interaction with a nucleon. As a result, the corresponding flavor charged lepton is produced, together with a different nucleon. An example is given by $\nu_\mu + n \to \mu^- + p$. The process is implemented in GENIE by means of the Llewellyn-Smith model [81], where the hadronic weak current is expressed in terms of the most general Lorentz-invariant form factors. In the case of nuclear targets, GENIE includes a suppression factor, taken from an analytic calculation of the rejection factor in the RFG model, based on the simple requirement that the momentum of the outgoing nucleon exceeds the Fermi momentum for the hit nucleus.
In the parametrization, both pseudo-scalar and axial vector are present. The pseudo-scalar form factor is expressed according to the partially conserved axial current (PCAC) hypothesis [81], while the axial form factor is fixed at

[1]The name EMC comes after the European Muon Collaboration, who discovered the effect in 1983 [79].

$Q^2 = 0$ by neutron beta decay measurements and the Q^2 dependence is taken by neutrino experiments. A dipole structure is assumed for the form factors.

NC elastic scattering keeps the initial particles unchanged after the interaction, with momentum transfer only. The process is implemented in GENIE according to the parametrization reported in [82] and the axial form factor has the form

$$G_A\left(Q^2\right) = \frac{1}{2}\frac{G_A(0)}{\left(1 + Q^2/M_A^2\right)^2}(1+\eta). \tag{4.1}$$

The parameter η includes possible isoscalar contributions to the axial current and the GENIE default value is $\eta = 0.12$. For nuclear targets the same suppression factor as for the QE case is used.

Baryon resonance production (RES) contributes mostly between 1 and 10 GeV. It consists of the excitation of a baryonic state within the nucleus, resulting in the production of a baryon (p or n, most of the time) plus a meson. GENIE employs the Rein-Sehgal model [83] both for CC and NC resonant interactions.

Coherent neutrino-nucleus scattering is a channel in which the neutrino interacts with the nucleus as a whole. As a result, pions are produced in the final state, both in the CC and in the NC interactions. The interaction is simulated according to the Rein-Sehgal model [84], updated with some modifications [85]. The coherent neutrino-nucleus scattering has a very low cross-section compared to the other processes and has been experimentally observed only recently [86].

Deep inelastic scattering (DIS) involves the interaction of a neutrino with the partons inside the nucleon, resulting in the nucleon fragmentation. To get a direct neutrino-parton interaction, the neutrino energy must be sufficiently high (≥ 1 GeV) and DIS becomes the dominant channel above $\sim$10 GeV. The process is calculated in an effective leading order model, employing the modifications in [80] to describe scattering at low Q^2. The cross-sections are computed including all valence and sea quarks in $\nu + q \rightarrow \nu/\ell + q'$. A scale factor of 1.032 is applied to the predictions of [80], to achieve a better agreement with the measured value of the neutrino cross-section at high energy (100 GeV).

Neutrino-electron elastic scattering is a sub-dominant channel at the energies here considered (≥100 MeV). The process involves the scattering of a neutrino out of an electron, via the exchange of a Z boson (all flavors) or a W boson (ν_e only). The cross-sections for all $\nu - e$ scattering channels are computed according to the review in [87].

A comprehensive review of neutrino interactions is reported in [24]. In fig. 4.2 are reported the cross-sections predictions for ν_μ-nucleon interaction in the dominant channels, together with some experimental results.

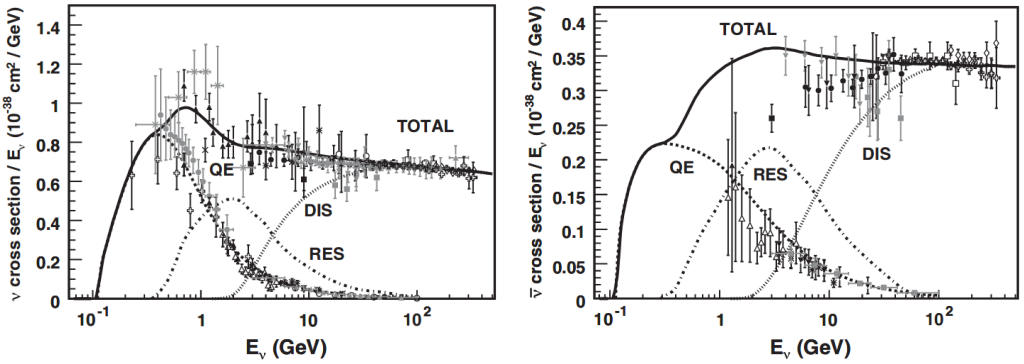

Figure 4.2: Total ν_μ (left) and $\overline{\nu}_\mu$ (right) per nucleon CC cross sections (for an isoscalar target) divided by neutrino energy, as a function of neutrino energy. Some experimental measurements are also reported. Separately are reported the contribution from QE (dashed), RES (dot-dashed) and DIS (dotted). Figure from [24].

The GENIE version used in this work is V2_12_10, released in 2018. The elemental composition of the JUNO LS has been set as neutrino target (almost entirely ^{12}C and ^{1}H).
The most stringent limitation to the total number of events and to the upper energy bound is the computational resources needed. The full simulation of neutrino interactions, and particularly the propagation of secondaries (described in the next section) requires a very large computational time. In fig. 4.3 is reported the distribution of the visible energy of secondary products of neutrino interactions, for ν_μ/ν_e CC and NC processes. The quantity is estimated as the kinetic energy of secondary particles. In the CC case, it is computed as the sum of kinetic energy of the hadronic part plus the final lepton, while in the case on NC events the hadronic part only is taken into account. The mass contribution is included for antibaryons[2].

[2]In order to get a more accurate estimation of the energy released in the LS, the mass

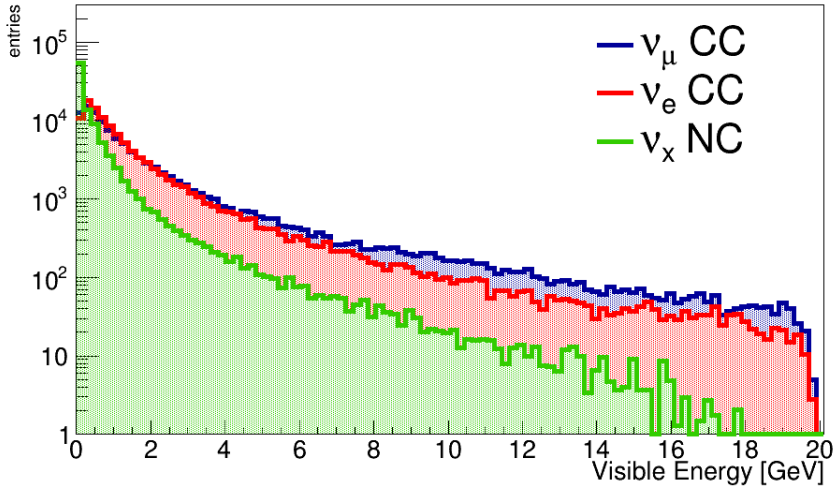

Figure 4.3: Distribution of the estimated visible energy of secondary particles after a neutrino interaction in the JUNO LS. The distribution is plotted separately for ν_μ CC (blue), ν_e CC (red) and NC (green) events.

4.3 Detector simulation

The JUNO detector simulation (*Detsim*) has been developed within the SNiPER framework [88], based on GEANT4 [89–91]. The SNiPER body is built on C++, while Python is used as user interface.
The Detsim takes the GENIE interaction vertices, containing all the secondary particles, and propagates them inside the detector. The GEANT4 libraries are able to simulate all the physical processes related to energy loss and scintillation. In the Detsim, several physics processes are implemented through GEANT4: electro-magnetic interaction, decay, hadron elastic and inelastic interactions, scintillation (including re-emission), Cherenkov emission and optical absorption.
After the neutrino interaction and the production of secondaries, the output scintillation photons can undergo absorption, re-emission, scattering, according to the optical model implemented in the Detsim. The simulation includes the photon propagation to the PMTs, the interaction with the photo-cathode and the production of PEs, by embedding the PMTs QE. The PE production after a photon interaction on the photo-cathode is referred to as a *hit*. As

of unstable particles too (e.g. $\pi^0 s$) should be considered in the computation. Fig. 4.3 is intended only to give an overall picture of the interaction channels inside the detector.

an example, in fig. 4.4 is reported the map of hit SPMTs after a neutrino interaction.

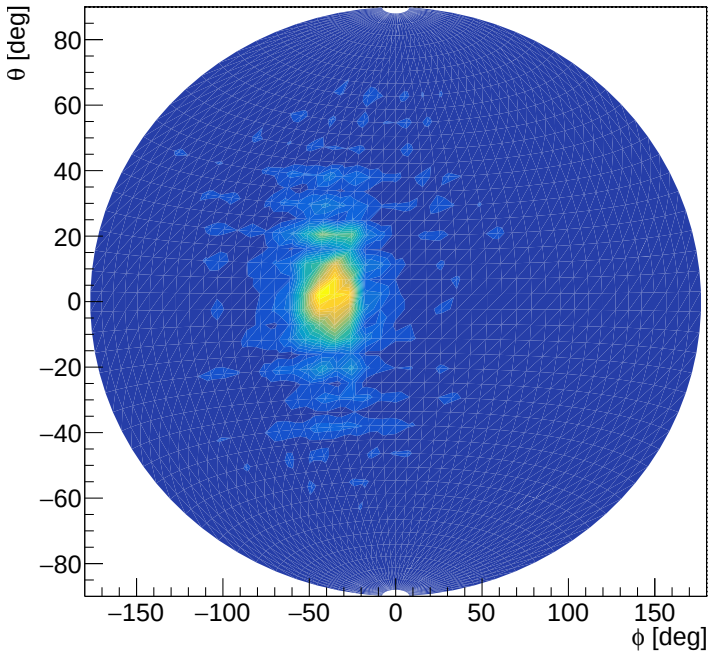

Figure 4.4: Hit map distribution on the SPMT system of a ν_e CC event inside the CD. The neutrino energy is ∼900 MeV. The coordinates are given in terms of the zentih (θ) and azimuth (ϕ) angle.

Since the JUNO detector is still under construction and no data is yet available, an independent MC sample has been generated as real data. The sample corresponds to roughly 5 years of detector livetime and the generation process has been the same as for the large sample described so far, concerning the flux model, the neutrino interaction generator and the detector simulation. The energy range [0 - 20 GeV] is also the same. The expected rate of atmospheric neutrino events in JUNO is around 2 - 3 events/day.

Chapter 5

Neutrino flavor identification and sample selection

The atmospheric neutrino events are selected in order to get two separate samples, one enriched in ν_e and the other one in ν_μ, with a good energy resolution on the final products of neutrino interactions. From the detector description in Chap. 3, it follows that JUNO is essentially a large calorimeter, which therefore achieves its best results in events which are entirely contained within the CD volume. The dense instrumentation and the high light output of the LS ensure excellent performances in reconstructing the energy of events.
The series of selections which are described in this chapter are therefore tuned to select those events whose secondaries start and end within the CD, here called fully-contained (FC). On the contrary, events which have some secondary particles escaping from the CD are defined partially-contained (PC) and exhibit a worse energy resolution. Through-going muons that may come from neutrino interactions outside the detector are not considered in the analysis. The above criteria form an intrinsic limitation for the spectrum reconstruction of high-energy ν_μ, namely $E_{\nu_\mu} \gtrsim 10\,\mathrm{GeV}$, because the resulting muon from a CC interaction is never fully contained inside the CD. The selection criteria have been tuned also to reject the cosmic muon background, made of high-energy events that can contaminate the neutrino sample.
The composition of the neutrino sample, as a function of the energy and according to the flavor and the topology (FC or PC) is reported in fig. 5.1. As already mentioned, the PC sub-sample is almost entirely composed of high-energy ν_μ CC interactions.
The selection criteria are applied to neutrino sample in two steps. The first selection is performed through fiducial cuts, targeted to remove edge events which may be badly reconstructed and the cosmic muon background. The

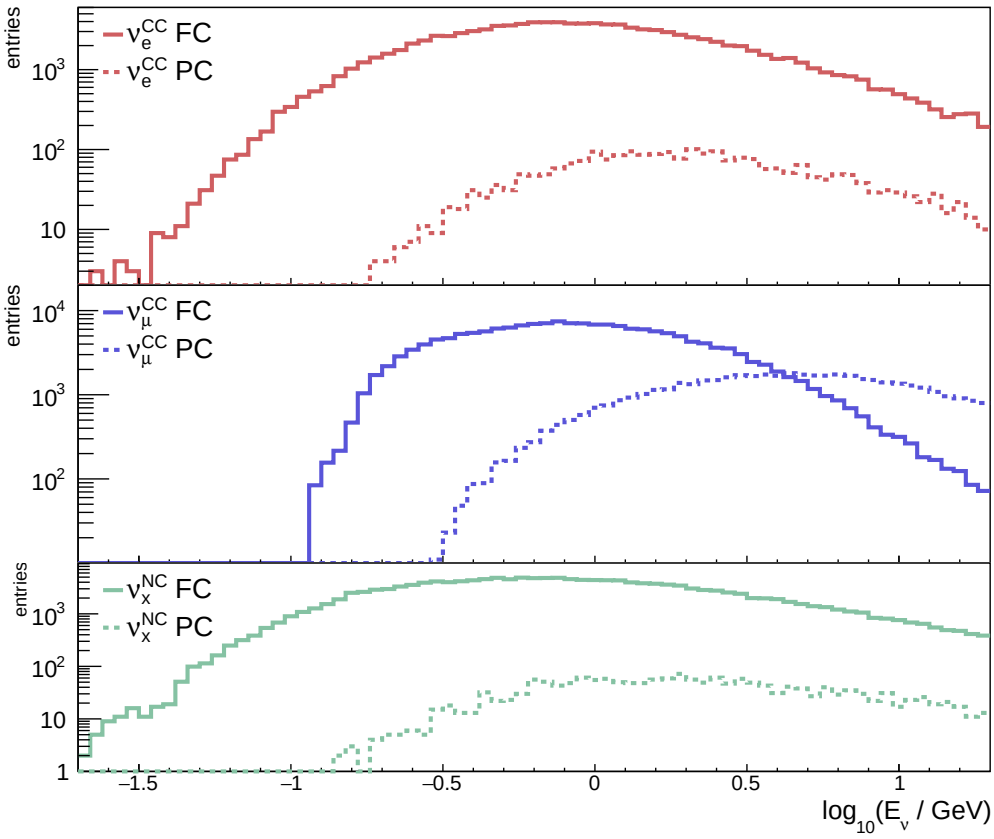

Figure 5.1: Energy distribution of neutrino events, for each sub-sample. Top: ν_e CC events; middle: ν_μ CC events; bottom: ν_x NC events. Full line: fully-contained events; dashed line: partially-contained events.

second selection is based on the time profile of the events and is applied for the flavor separation.

5.1 Fiducial cuts

In order to make a preliminar selection and remove PC, cosmic muon and edge events, a set of two fiducial cuts are applied to the sample:

$R_{VERTEX} < 16\,m$. The cut on the vertex position is applied in order to remove events which release their energy near the edge of the acrylic sphere. This class of events tipically show a deviation in the linear relationship between the true energy and the reconstructed one, for two main reasons: first, part of the energy is released in the acrylic

and not in the LS; second, the closest PMTs collect a great amount of light and can undergo saturation. In fig. 5.2 is reported the ratio between the number of PEs (NPE) on the LPMT system in the CD and the visible energy, as a function of the cube of the true vertex radius. Unless specified, from here onwards NPE refers to the NPE collected by the LPMT system of the CD.
The R_{VERTEX} represents the vertex radius, i.e. the distance between the vertex and the center of the sphere. In order to reproduce the uncertainty on the reconstructed vertex position $\overrightarrow{\rho}_{RECO}$, the true MC position $\overrightarrow{\rho}_{TRUE}$ has been modified as:

$$\overrightarrow{\rho}_{RECO}(x', y', z') = \overrightarrow{\rho}_{TRUE}(x, y, z) \oplus f_{GAUS}(\sigma = 1m), \tag{5.1}$$

where f_{GAUS} is a gaussian function, with a variance $\sigma = 1\,\mathrm{m}$. The estimated performances of JUNO on $\mathcal{O}$(MeV) events is as little as a few cm. However, in the case of high energy events like atmospheric neutrino interactions, the performances can become as worse as $\mathcal{O}(1\,\mathrm{m})$, as estimated from preliminary studies within the collaboration.

$\mathbf{NPE^{WP} < 60}$. The cut on the total charge collected in the WP is used to reject cosmic muon events and PC neutrino events.

Fiducial cuts can be seen as quality cuts, since they aim to remove poorly reconstructed events. The efficiency of fiducial cuts on the neutrino sample is reported in table 5.1, singularly and combined together.
After the selection, the neutrino sample is composed at 97% of FC event, calculated on the MC sample. The remaining PC events are composed at 96% of ν_μ CC interactions. The efficiency on the cosmic muon rejection is the subject of Sec. 5.3.

Selection	$\boldsymbol{\nu_e}$	$\boldsymbol{\nu_\mu}$
$\mathbf{R_{VERTEX} < 16\,m}$	74%	74%
$\mathbf{NPE^{WP} < 60}$	99%	92%
Total	73%	68%

Table 5.1: Summary of fiducial cuts efficiency on the ν_e and ν_μ sample. The values are reported for the single cuts alone and combined together.

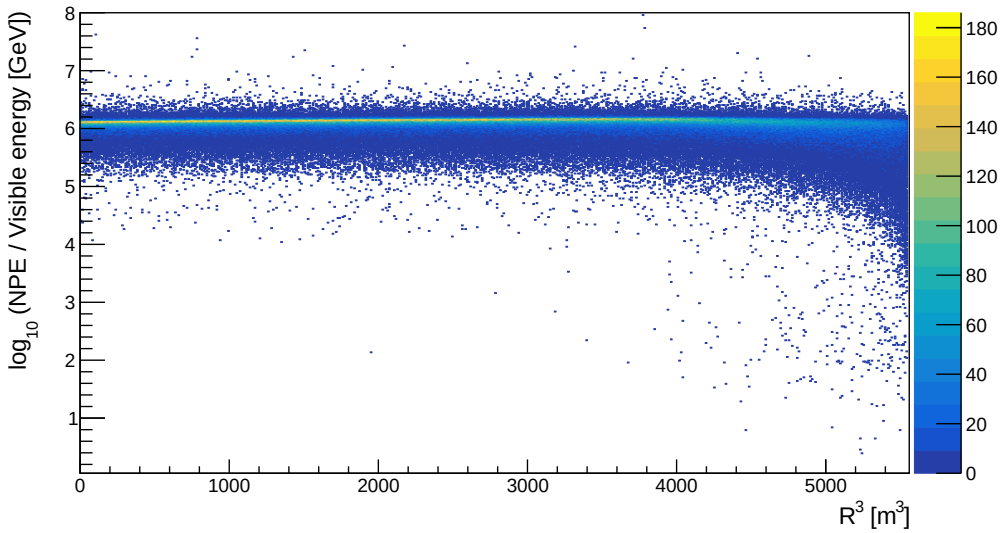

Figure 5.2: Linearity response of JUNO as a function of the vertex distance from the center. On the X axis is reported the cube of the vertex radius, to get an equal number of events per volume unit. On the Y axis is reported the log of the ratio between the collected NPE and the visible energy of the event (in GeV). Note that 16 m correspond to approximately 4000 m^3.

5.2 Time residual-based discrimination

As already mentioned above, the CC interactions constitute the preferred channel for neutrino flavor identification. ν_e and ν_μ generate respectively a $e^\pm$ and a $\mu^\pm$, which have different behaviours. Electrons lose their energy quickly, via bremsstrahlung and ionization and even at $\mathcal{O}$(GeV) energies they are unable to travel for more than 1-2 meters.
On the other side, muons with energy > 1 GeV travel in general for a longer distance inside the detector with respect to electrons, because they are often around the minimum ionizing power (MIP) point. Additionally, low-energy muons decay inside the scintillator volume, giving rise to a delayed energy release from the Michel electron. The above differences make ν_μ CC events quite prolonged in time with respect of ν_e CC events, which indeed appear more point-like. Hadronic particles are common to all events and compose all the visible part of NC events. Hadrons have in general a long-living energy release, because of interactions and decays.
The different temporal behaviour of the classes of events has been exploited by building a time profile-based discrimination algorithm [92]. The SPMT

system has been used in the algorithm, since it is more accurate in time measurement. To realistically reproduce the effects produced by TTS, a gaussian smearing has been applied to the true hit time over every SPMT. Measurements ongoing within the collaboration (with a larger statistics than in [67]) show that typical TTS value for JUNO SPMTs are below 4 ns. To be conservative, the gaussian function used for the time smearing has a variance $\sigma = 4$ ns.
A hit time-residual is defined for each SPMT as:

$$t^i_{res} = t^i_{hit} - \left(\frac{n \cdot R^i_V}{c}\right) \tag{5.2}$$

where t^i_{hit} is the hit time on the i-th SPMT, c/n is the speed of light inside the scintillator and R^i_V is the distance between the i-th SPMT and the interaction vertex. The reconstructed vertex position is used. As an example, in fig. 5.3 the t_{res} distribution of two CC events are shown, where the secondary peak due to the Michel electron is clearly visible.

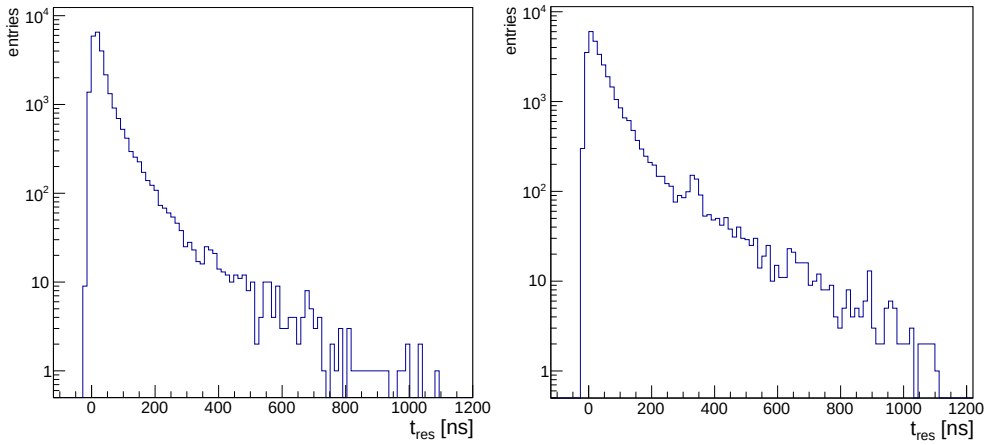

Figure 5.3: Example distribution of the t_{res} variable for two events. Left: ν_e CC event, with E_ν ~1.5 GeV; right: ν_μ CC event, with E_ν ~2 GeV. The secondary peak at t_{res} around 300 ns in the right plot, due to the Michel electron, is clearly visible.

Since ν_μ and ν_e CC events result in different light production duration, the RMS of the t_{res} distribution is used as a discrimination variable (here called $\sigma(t_{res})$). Neutrino events are considered in the NPE interval $[1.0 \cdot 10^5 - 1.58 \cdot 10^7]$, to remove the low-energy core of NC events and to stay sufficiently far

from the MC generation edges.
In fig. 5.4, the $\sigma(t_{res})$ distribution is reported for the three populations: ν_μ CC, ν_e CC and NC events. The variable is also reported separately in 4 different bins of NPE, selected in order to have equal statistics in each bin.

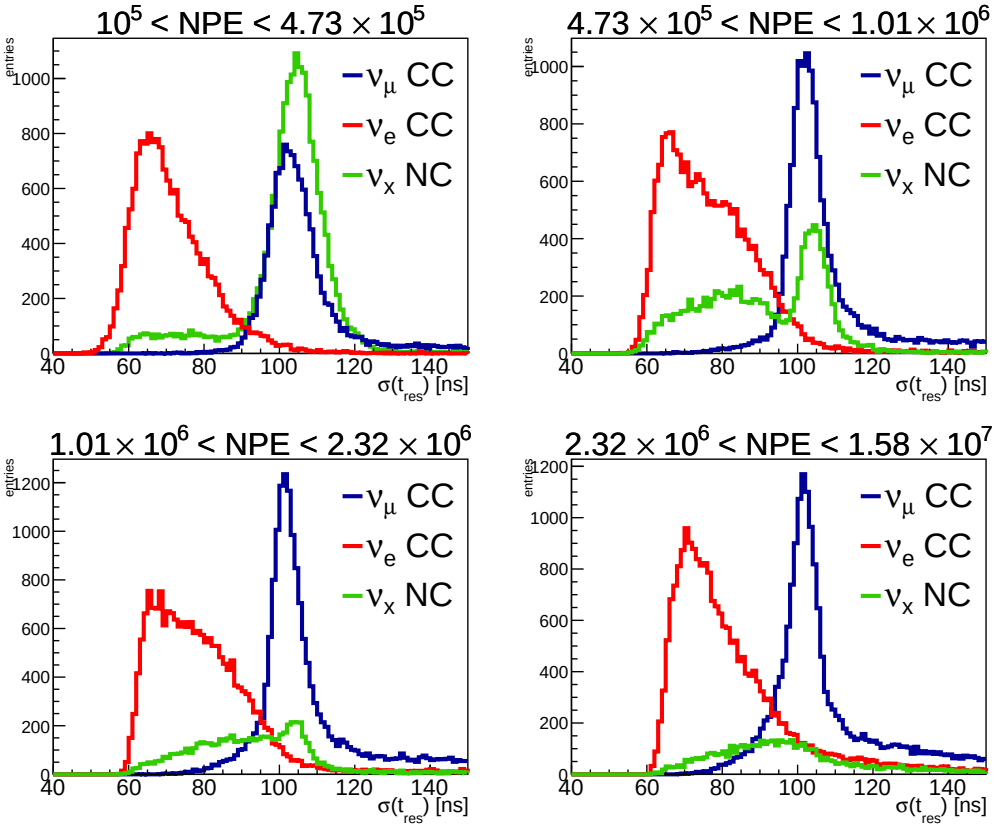

Figure 5.4: Distribution of $\sigma(t_{res})$ for ν_μ CC (blue), ν_e CC (red) and NC events (green). The NPE range is reported above the figures.

The plots in fig. 5.4 show a good isolation of the ν_e CC component, over the whole energy range. On the contrary, the ν_μ CC and the NC components appear to be overlapped. The hadronic part of the secondaries has indeed an important contribution from charged pions, which decay with ∼100% probability into $\mu+\nu$. Also protons and neutrons have timing feature similar to muons, because they scatter for a long time before stopping. All these channels are therefore an irreducible background for the ν_μ analysis. The NC component contribution, however, becomes less significant at high energy, because of the steeper spectral shape (fig. 4.3).
The vertex resolution could in principle have an influence on the computed

value of $\sigma(t_{res})$. As previously explained, the resolution effects are taken into account by smearing the original vertex position. In fig. 5.5 the modification of the $\sigma(t_{res})$ value is reported, as a function of vertex displacement with respect to the true one. The net spread remains within a few ns, showing a little influence of the vertex resolution on the $\sigma(t_{res})$ value.

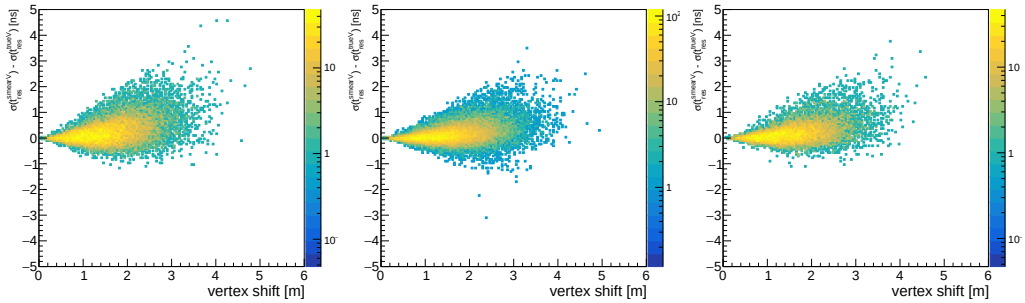

Figure 5.5: Net difference between the values of $\sigma(t_{res})$ calculated with respect to the reconstructed vertex and the true one, as a function of the distance between the true and the reconstructed vertex. The plots are displayed separately for the ν_e CC sample (left), the ν_μ CC sample (center) and the NC sample (right), after fiducial cuts.

Given the different features of neutrino populations in fig. 5.4, two separate phase space selections for the energy spectrum reconstruction are applied, for ν_e and ν_μ. The target is to isolate CC events, which allow to discriminate the neutrino flavor. The residual NC events, which have not been removed by the t_{res} selection, are populated both of ν_e and ν_μ.

ν_e selection

In order to isolate ν_e events, a value of $\sigma(t_{res}) < 75\,\text{ns}$ is required. The cut results in an efficiency for ν_e events $\simeq$35% with respect to the sample after fiducial cuts and a residual contamination from ν_μ less than 6%. The NPE distribution of ν_e is reported in fig. 5.6 - left, including all the selections sequence.

ν_μ selection

Since the ν_μ CC sub-sample is strongly contaminated from NC events at low energy, a further requirement of NPE $> 5 \cdot 10^5$ is set, which converts to approximately 400 MeV. A requirement of $\sigma(t_{res}) > 95\,\text{ns}$ is then performed. The efficiency for ν_μ events is 50% with respect to the sample after fiducial

cuts. The residual ν_e contamination is less than 20%. The NPE distribution of ν_μ is reported in fig. 5.6 - right, after every selection step.

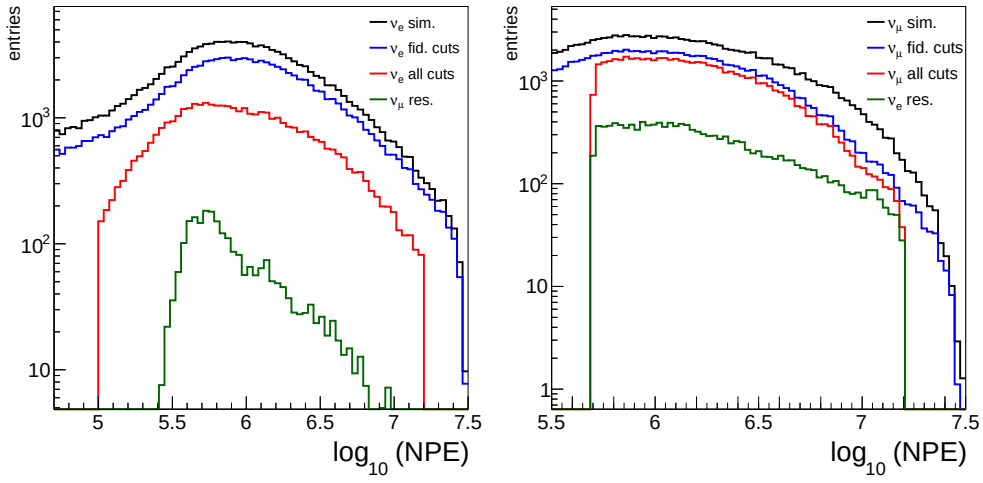

Figure 5.6: NPE distribution of neutrino sample after the selection process, for ν_e (left) and ν_μ (right). The generated spectrum is in black; the spectrum after fiducial cuts is in blue; the spectrum after the full selection chain, including the $\sigma(t_{res})$ cut, is in red; the residual wrong-flavor spectrum after all selections is in green.

5.3 Cosmic muon background

The cosmic muon background consists of the secondary muon flux produced after the interaction of Cosmic Rays with the atmosphere, in the same way as for the neutrino flux. Although the JUNO detector location is about 700 m underground, part of the muon radiation is able to penetrate the rock overburden and release energy inside the detector. The energy and zenith angle distributions of cosmic muons entering inside the JUNO detector are reported in fig. 5.7.
The energy released by cosmic muons inside JUNO is comparable with that of particles coming from atmospheric neutrino interactions (hundreds of MeV - several GeV). Muons can mimic the topology of atmospheric neutrino events and can be therefore a source of background. Although the external water Cherenkov veto is designed to reject these events with high efficiency, the cosmic muon event rate is several orders of magnitude higher than that

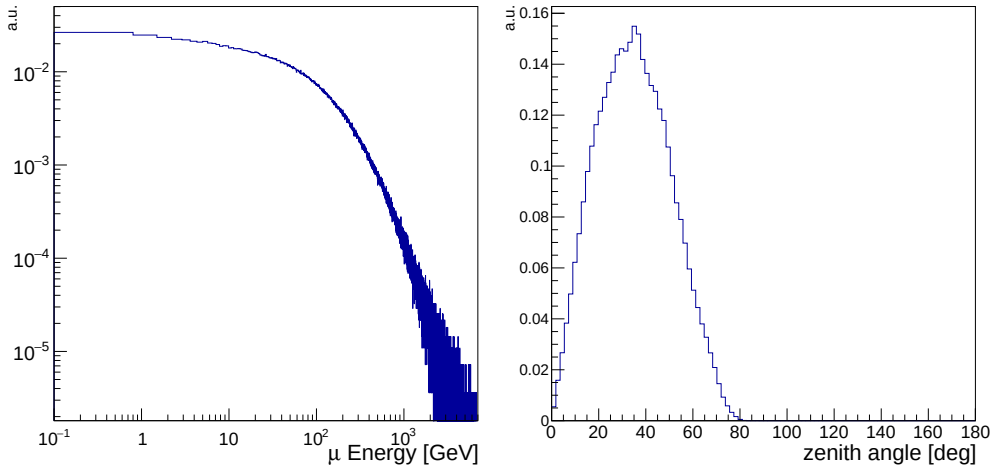

Figure 5.7: Energy (left) and zenith angle (right) distributions of cosmic muons arriving to the detector, in arbitrary units. Muon flux has been generated according to a modified Gaisser parametrization [93] and propagated through matter with the MUSIC software pakage [94]. The mountain profile above the JUNO site is included. The simulation has been perfomed within the collaboration and is not part of this work.

from atmospheric neutrino interactions. From preliminary calculations, their event rate inside the JUNO CD is around 3 - 4 Hz, corresponding to roughly 10^5 the neutrino event rate. The desired rejection rate for the cosmic muon background must be therefore at least below 10^{-5}.
In order to get a comprehensive picture of the cosmic muon flux within the framework of this study, a full MC simulation would be necessary. To reproduce a realistic event sample corresponding to some years of data-taking, $10^8 - 10^9$ events would be necessary. The deposited energy for each of these events is large and causes the production of many millions of photons. As a result, an extremely large CPU time and storage space would be necessary.
To overcome this issue, a 2D toy MC model has been built. It implements a simplified geometry of the JUNO detector, including both the CD and the WP. Muons are injected according to the energy distribution in fig. 5.7 - left and all the processes related to light production and attenuation are simulated, including stochastic fluctuations. The energy loss of muons inside water and LS is parametrized according to the tables from [4]. The refractive indexes and the attenuation lengths of photons used are the same of the JUNO Detsim, as well as the material densities. The PMTs are parametrized as an active surface where photons can be detected, by using the PDE values

measured in [65].
The toy model is able to reproduce the WP veto performances, for cosmic muons, obtained with the full MC simulation of the WP only. If a simple PMT majority trigger is used, the muon tag efficiency is about 98%.
Cosmic muons appear to the JUNO detector as high-energy tracks which release a large amount of energy both in the WP and in the CD. The fiducial cuts described in Sec. 5.1 require instead a large amount of light inside the CD and a low collected charge inside the WP. By applying the same fiducial cuts to the muons generated with the toy MC, a rejection power $< 1.15 \cdot 10^{-6}$ at 90% confidence level is achieved.

Chapter 6

Atmospheric neutrino energy spectrum

The atmospheric neutrino energy spectrum can be inferred from the detector observables. Although experimental observations in the low energy region of the atmospheric spectrum has been performed in the past [37, 45], some miscrepancies survive. Furthermore, the improvement in the knowledge of the energy spectrum results also in a better understanding of neutrino oscillation effects and in more effective predictions about rare processes searches, like the proton decay. In this last case, low-energy atmospheric neutrino events are an important source of background [58, 95]. The characterization of the atmospheric neutrino flux helps also the study of low-rate astrophysical sources, like the relic supernovae neutrino flux, for which atmospheric NC events can mimic the signal topology [58].
In this section, the technique adopted to reconstruct the atmospheric neutrino flux is described. The analysis is performed both for the electron and the muon neutrino flux, which are extracted separately. An evaluation of the uncertainties impact on the final reconstructed spectra is also reported.
The energy spectrum reconstruction embeds the base issue of finding a relationship between the measured quantities and the energy of the neutrino which interacted inside the detector. The issue is not trivial, since the experimental observables are affected by wide fluctuations, coming from the probabilistic nature of the processes which regulate the development of the secondaries. The event reconstruction must also take into account factors like the efficiency of the detector. In general, the issue of correlating quantities which do not have a direct relationship, but instead a statistical one, is addressed by means of *unfolding* techniques.

6.1 Spectrum unfolding

The JUNO electronic image of a neutrino event provides different quantities: among them, a fundamental role is played by the total number of photo-electrons collected by the PMT system, which is an estimation of the total energy released by secondary particles. In this study, the NPE on the CD LPMT system is used as deposited energy estimator. In order to match the effective distribution which is acquired by the DAQ system, the hits in the first 1.2 μs only are considered. From a set of events, this NPE distribution is produced and can be expressed in general as:

$$N(NPE) = \int \Phi(E_\nu)\ A_{eff}(E_\nu, NPE, \Omega, T, \ldots)\ \varepsilon(T, NPE \ldots)\ dE\ d\Omega\ dT, \tag{6.1}$$

where T is the data acquisition time, Ω is the is solid angle which defines the detector acceptance, ε is the detector efficiency and A_{eff} is the effective area for the event detection. The value of the primary neutrino flux $\Phi(E_\nu)$ is evaluated according to hypothesis, by comparing the measured spectrum with theoretical predictions which undergo the same reconstruction process. In this study, an unfolding method is adopted to reconstruct the primary energy spectrum. The advantages of this class of methods is that the unfolded spectrum is directly compared to the observable one, without any assumption on the primary distribution. The observable spectrum M_j is therefore unfolded into the true neutrino energy spectrum N_i, where the subscripts i and j denote respectively the binning of the n_E causes ($i = 1,\ldots,n_E$) and the n_M effects ($j = 1,\ldots,n_M$). Concerning the observable distribution, the binning is defined as follows:

$\boldsymbol{\nu_e}$ sample: 7 bins equally spaced in $\log_{10}$(NPE), from 5.0 to 7.2.

$\boldsymbol{\nu_\mu}$ sample: 8 bins equally spaced in $\log_{10}$(NPE), from 5.7 to 7.2.

The unfolded spectrum binning is indeed defined as follows:

$\boldsymbol{\nu_e}$ sample: 7 bins equally spaced in $\log_{10}(E_\nu$ / GeV), from -1.0 to 1.05.

$\boldsymbol{\nu_\mu}$ sample: 7 bins equally spaced in $\log_{10}(E_\nu$ / GeV), from -0.3 to 1.05.

The observable spectrum can be expressed in terms of the primary spectrum which originated the events:

$$M_j = \sum_i A_{ji} N_i, \tag{6.2}$$

where A_{ji} is the detector likelihood matrix, which can also be identified as the conditional probability that a neutrino with a certain energy produces a certain amount of NPE: $A_{ji} = P\left(NPE|E_{\nu_i}\right)$. The A_{ji} matrix is estimated from the MC and represents the detector response. The (6.2) can be inverted and the primary spectrum can be expressed as:

$$N_i = \sum_j U_{ij} M_j, \tag{6.3}$$

where U_{ij} is the unfolding matrix. In the same way, the unfolding matrix can be expressed as the conditional probability that an event which produced a certain amount of NPE originated from a neutrino with a certain energy: $U_{ij} = P\left(E_{\nu_i}|NPE\right)$. There are in general different methods to retrieve the unfolding matrix. The algebraic inversion of A is not indeed a proper approach, since unfolding is a probabilistic procedure and must be addressed by means of the laws of probability.

6.1.1 Bayesian approach

An iterative method, based on the Bayes Theorem, is used to evaluate the U matrix [96,97]. The detector likelihood matrix is estimated using the full MC sample and then normalized as $\sum_j A_{ji} = 1-\epsilon$, where ϵ takes into account the inefficiency due to the reduced phase space considered by the matrix. The wrong-flavor events are included in A_{ji} as a possible cause i. The unfolding matrix can be built through the Bayes Theorem as:

$$U_{ij} = \frac{A_{ji} P\left(E_{\nu_i}\right)}{P(NPE^{CD}_{LPMT_j})} = \frac{A_{ji} P\left(E_{\nu_i}\right)}{\sum_{k=1}^{n_E} A_{jk} P\left(E_{\nu_k}\right)}. \tag{6.4}$$

The quantity $P\left(E_{\nu_i}\right)$ is the probability to observe a neutrino with energy E_{ν_i} and is the quantity which is intended to be measured. Once an initial prior probability distribution $P_0(E_{\nu_i})$ is defined, a first estimation of the neutrino fluxes is performed through the (6.3). This estimation provides a result which combines the MC input and the data. In order to obtain a better estimation of the energy distribution, a series of iterations are implemented: the initial unfolded distribution is used to build a new prior, which generates new conditional probabilities, to eventually update the unfolded spectrum.
There is not a rule for the best number of iterations to be performed. In general, a low number of iterations may be influenced by the choice of the prior and may not fully consider all the information coming from data. On the other side, a high number of iterations enhances the statistical fluctuations of the data sample and may affect the shape of the unfolded spectrum [97].

The effect of the particular shape of the prior distribution is in general small and can influence the number of iterations needed for the convergence of the method [97]. Possible bias effects are taken into account in the evaluation of the systematic uncertainties of the unfolding method, which is discussed in Sec. 6.2. The prior should reflect in principle the best knowledge of the primary spectrum, so that the minimum bias is achieved by adopting the true MC distribution.
The iterative Bayesian method is therefore strongly data-driven and very good results are obtained after few iterations. In this work, 2 iterations are performed. A soft smoothing is applied to the first value of $P(E_{\nu_i})$. As prior distribution, the HKKM14 model is used [34]. The flux values at the i-th bin center are obtained by interpolation and the prior is normalized to the unity. The two unfolding matrices, for ν_e and ν_μ, are reported in fig. 6.1.

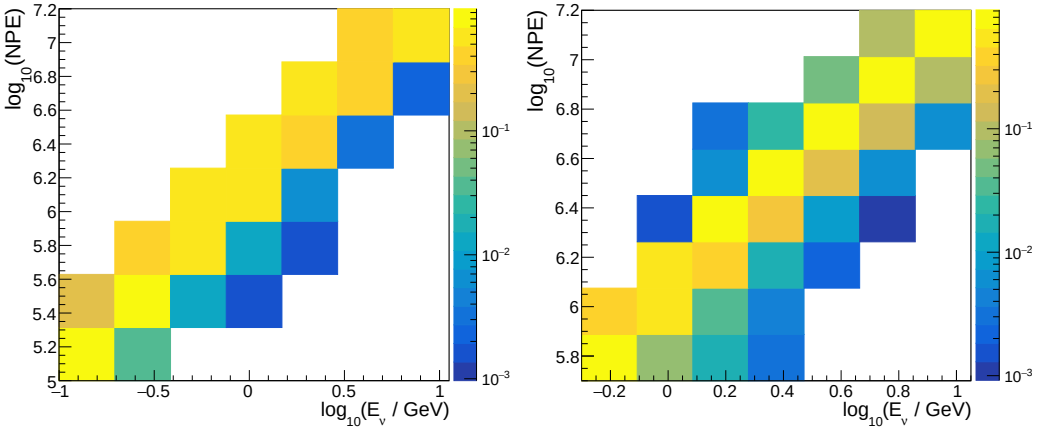

Figure 6.1: Unfolding matrices calculated with the full MC sample according to the (6.4), for ν_e (left) and ν_μ (right).

6.1.2 Simulated data sample

In order to test the JUNO performances in reconstructing the atmospheric neutrino flux, an independent MC sample has been generated, as explained in Chap. 4. The sample corresponds to a detector livetime of about 5 years and all the simulated events have been selected according to the criteria described in Chap. 5. Table 6.1 summarizes the sample population as a function of the flavor and the cuts applied. The event distribution of the sample, after the full selection chain, is reported in fig. 6.2 as a function of the observable NPE.

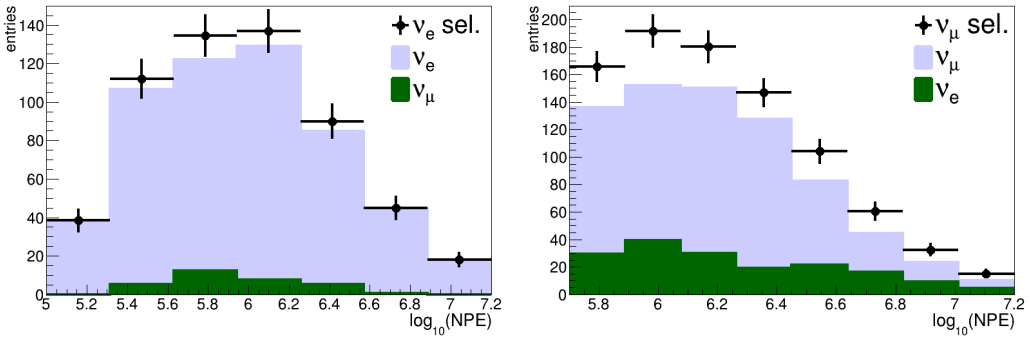

Figure 6.2: Distribution of the observable NPE in the corresponding bins, after the ν_e selection (left) and the ν_μ selection (right). The black dots represent the number of selected events in every bin j, with associated statistical error. The filled histograms reproduce the bin composition, in terms of the correct-flavor (light blue) and the wrong flavor (green).

The NPE bins reported in fig. 6.2 are hereafter referred to as "data bins" and the new MC sample as "data sample".

# of events	$\boldsymbol{\nu_e}$	$\boldsymbol{\nu_\mu}$
Bef. sel.	2049	2119
Fid. cuts	1484	1447
$\sigma(t_{res})$ cut	545	729
Res. bkg	31	173

Table 6.1: Summary of selections flow for ν_e and ν_μ fluxes, in terms of number of events, applied to the data sample. The values are reported before the selections, after the fiducial cuts and after the $\sigma(t_{res})$ selection. The residual background (i.e. wrong-flavor neutrino events) is also reported.

6.1.3 Reconstructed flux

In fig. 6.3 the spectra for the ν_e and ν_μ fluxes obtained from the data sample are reported. The uncertainties on the flux values are explained in next section. The predicted HKKM14 flux [34] is also reported, both at the source and including oscillation effects along the baseline. The flux deficit in the ν_μ flux below 10 GeV is clearly visible.

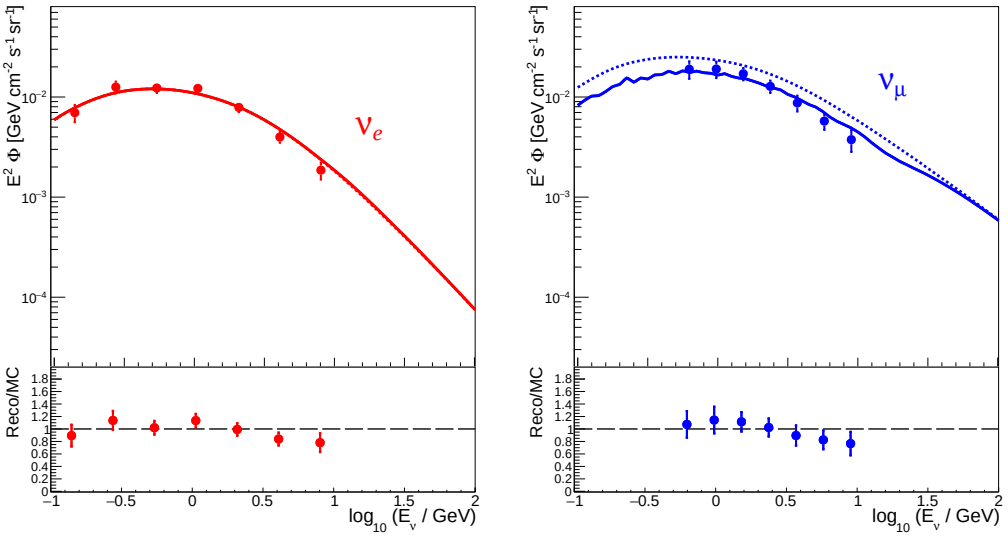

Figure 6.3: Reconstructed energy spectra for the ν_e (left) and the ν_μ flux (right). The fluxes are plotted multiplied by E^2, to give a better picture. The error bars on the flux values include all statistical and systematic contributions evaluated in Sec. 6.2. The HKKM14 flux prediction [34] is also reported, at the source (dashed line) and including the oscillation effects (full line).

6.2 Uncertainties evaluation

In order to evaluate the total uncertainty on each measurement bin, several contributions are considered. Both the statistical and the systematic uncertainties are included, from different sources. Among the systematics, the contribution from the unfolding method, oscillation parameters, analysis cuts and neutrino-nucleon cross section are considered.

Statistical uncertainty

The statistical uncertainty is due to the stochastical fluctuations that occur in the data bins. The amount of this fluctuations is visible in fig. 6.2, for each observable bin. In order to evaluate their impact in the final unfolded spectrum, 1000 toy pseudo-data have been generated, each time varying the bin content according to a poissonian distribution. The final distribution in the unfolded spectrum (fig. 6.4) is then fitted by means of a gaussian function, whose σ is quoted as the statistical uncertainty.
The statistical contribution ranges from 5% in the bins with highest statistics

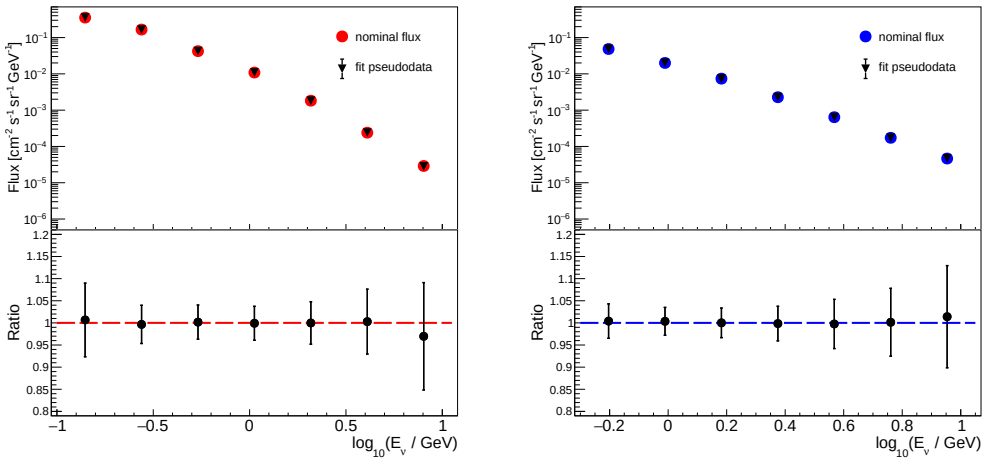

Figure 6.4: Up: unfolded spectrum (red/blue dots) and gaussian fit on pseudo-data from stochastical fluctuations (black triangle); down: fit-unfolded spectrum ratio, with the corresponding uncertainty. Left: ν_e spectrum; right: ν_μ spectrum.

up to $\sim$15% in the highest-energy bins.

Effects of the selection criteria

The selections procedure is in general desired not to produce any bias on the final sample. As explained in the previous chapter, fiducial cuts consists of quality selections applied to the neutrino sample. Their impact is visible in fig. 5.6. The final selected spectrum is well contained inside the fiducial cuts interval, so that the fiducial cuts values do not affect the flux reconstruction. The time residual-based selection, on the other hand, could bring some bias in the data bins where the statistics is low: an even small variation in the chosen cut value of $\sigma(t_{res})$ could result in a substantially different value of the unfolded flux, due to the wide stochastical fluctuations. The whole analysis has been therefore performed by varying each time the nominal cut value of $\sigma(t_{res})$ in a [-5 ns, +5 ns] time window and in 1 ns steps. The output spectra are reported in fig. 6.5.
The differences in the unfolded flux are relevant in the bins with less statistics, for the reasons explained above. The total contribution to the bin uncertainty is evaluated as the standard deviation of the flux values distribution in each bin.

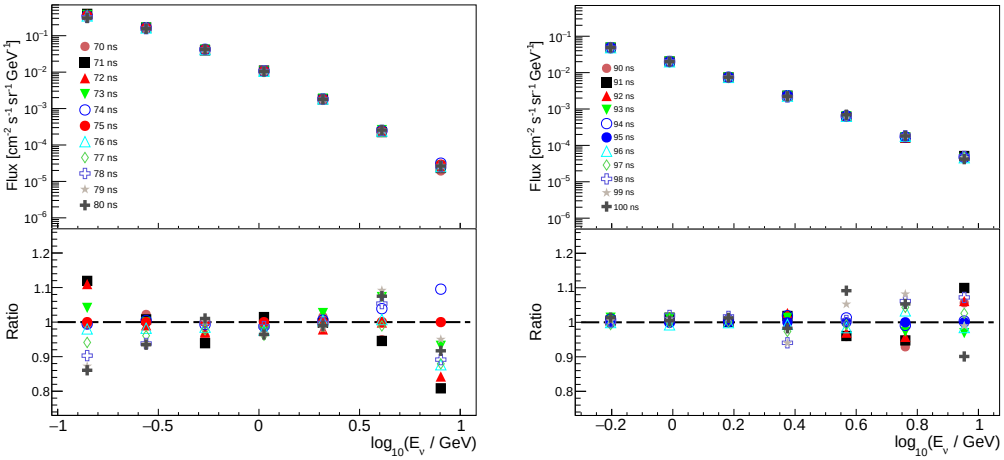

Figure 6.5: Up: unfolded spectra for the corresponding cut value on $\sigma(t_{res})$; down: Ratio between each top spectrum and the one used in the analysis. Left: ν_e spectra; right: ν_μ spectra.

Oscillation parameters effects

The current uncertainties on the global fit oscillation parameters are reported in tab. 1.1, which are assumed to be gaussian. 1000 toy MC pseudo-data have been generated, randomly varying the oscillation parameters within the experimental uncertainties, including the mass ordering and assuming no correlation. The final distribution in the unfolded flux (fig. 6.6) is fitted in each bin by means of a gaussian function. Since the resulting dispersion is rather small in every bin, the total per-bin uncertainty contribution is quoted as the displacement of the distribution fitted peak with respect to the nominal flux value.
The total contribution from oscillation parameters uncertainty is estimated to be below 1% on the entire spectrum. The only exception is the first bin of the ν_μ spectrum, since oscillation effects are larger, where the uncertainty is quoted between 2% and 3%.

Cross-section uncertainties

The uncertainties on neutrino cross-section impact directly on the number of observed events. In the MC simulation process described in Chap. 4, neutrino interactions are managed by the GENIE software. The full list of uncertainty sources considered by GENIE is provided in [98] (pagg. 131,132).

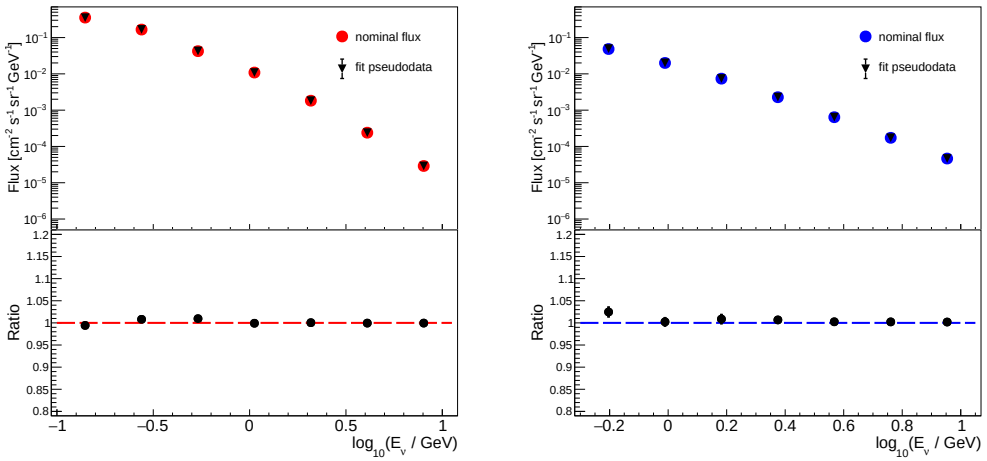

Figure 6.6: Up: unfolded spectrum (red/blue dots) and gaussian fit on pseudo-data from oscillation parameters random variation (black triangle); down: fit-unfolded spectrum ratio, with the corresponding uncertainty. Left: ν_e spectrum; right: ν_μ spectrum.

A comprehensive handling of the whole list is not trivial, since it requires the simultaneous calculation of modified interaction probabilities in a wide parameter space. In this study, the evaluation of the cross-section uncertainty is based on experimental measurements provided by the T2K Collaboration [99–101], extrapolated from the associated data releases. Assumed the uncertainty on the measured cross section values to be gaussian, the related visible spectrum is modified accordingly, within 1σ interval. The propagated uncertainty on the unfolded flux is evaluated by unfolding 1000 toy MC pseudo-data, using randomly modified NPE bin contents. The unfolded spectra distribution (fig. 6.7) are then fitted in each bin by means of a gaussian function, whose σ is quoted as the related uncertainty contribution. The uncertainty in the neutrino cross-section values has a large impact in the final reconstructed flux, up to 20%.

Uncertainty from the method

Although the iterative Bayesian unfolding method is data-driven, the particular MC sample may have an influence on the final result. This means that the initial estimation of the likelihood matrix may have an intrinsic bias, as well as the choice of the prior. The relative impact should be small but, as in the previous cases, it can be appreciable in the unfolding bins with low

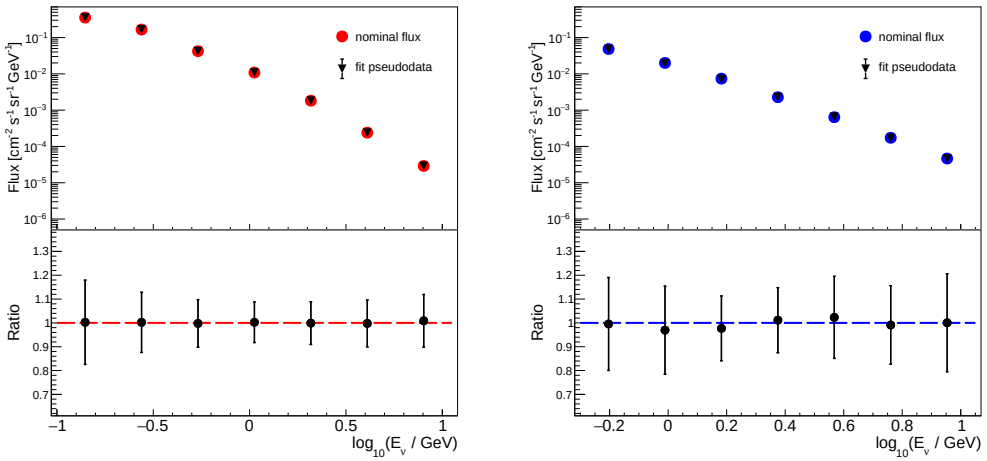

Figure 6.7: Up: unfolded spectrum (red/blue dots) and gaussian fit on pseudo-data from cross-section random variation (black triangle); down: fit-unfolded spectrum ratio, with the corresponding uncertainty. Left: ν_e spectrum; right: ν_μ spectrum.

statistics. The net effect cannot be exactly computed, but a reliable estimation can be achieved by unfolding modified data sets, generated by assuming a primary MC distribution reasonably far from the nominal one.
The modified unfolded spectra are produced from the original MC by means of a re-weighting procedure. The new spectrum can be expressed in the i-th unfolding bin as:

$$\Phi_{\nu_i}^{MOD} = (1+\alpha)\left(\frac{E_{\nu_i}}{1\,GeV}\right)^{\gamma}\Phi_{\nu_i}^{MC}, \tag{6.5}$$

where α acts on the absolute normalization and γ on the shape of the primary spectrum. These two parameters are considered to range in the following interval:

Parameter	Range of variation
α	± 0.05
γ	± 0.2

Table 6.2: Variation intervals considered for the α and γ parameters.

The size of variation corresponds approximately to a 1σ uncertainty interval in the predicted spectra (see [102], pag. 25).

In fig. 6.8 the ratio of the modified spectra and their corresponding unfolded flux is reported, together with the per-bin fractional deviation between the input and the unfold.

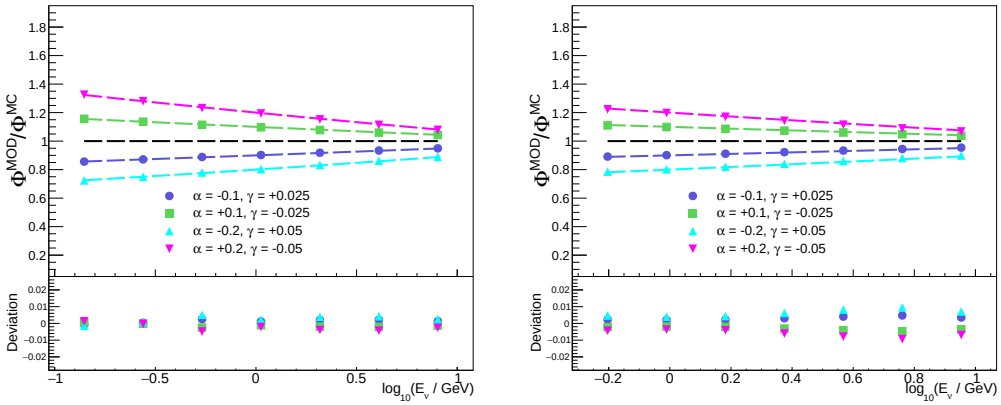

Figure 6.8: Modified unfolded spectra, together with the corresponding input (up) and their relative ratio (down). Left: ν_e spectra; right: ν_μ spectra. Φ^{MC} represents the nominal flux model [34]. Four sets of modified spectra are plotted, whose α and γ values are reported in the figures.

The deviation introduced by modified spectra are below 1% in most cases and slightly above, in the case of maximum variation of α and γ, in the bins with low statistics only.

Uncertainties summary

The contributions of each uncertainty source are reported in fig 6.9, for each unfolding bin. The total uncertainty reported is calculated as the root of the square sum of all the contributions. The neutrino cross-section uncertainty represents the dominant contribution over the whole unfolded spectrum, with an important contribution coming also from statistics. The total flux uncertainty ranges from a minumum value of 10-15% in the $\mathcal{O}(1\,\text{GeV})$ energy region, up to a 20-25% in the edge bins.

6.3 Results and discussion

In fig. 6.10 the reconstructed spectra for ν_e and ν_μ are presented, compared with the measurements provided by other experiments. JUNO is able to reconstruct the energy spectrum of atmospheric neutrinos in the energy

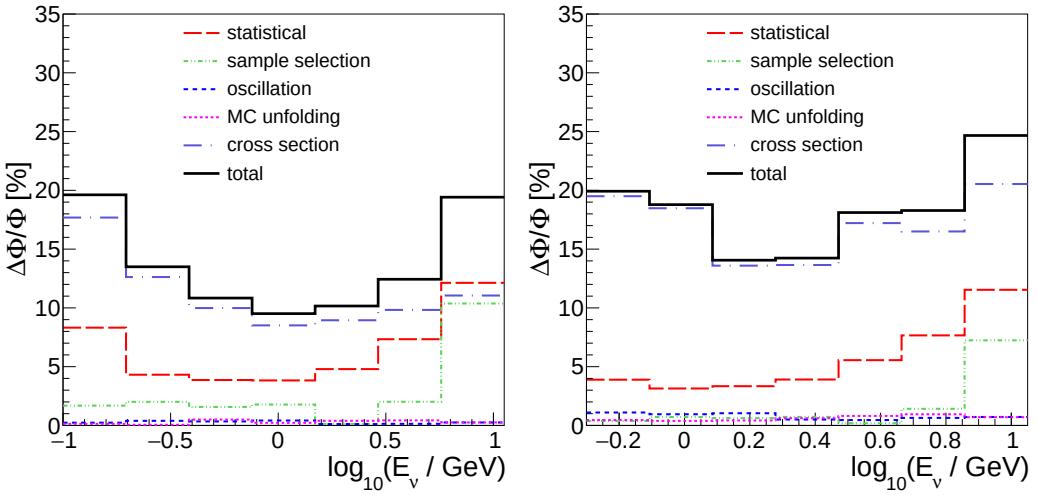

Figure 6.9: Summary of estimated relative uncertainty on the unfolded flux, reported separately for each source. The total relative uncertainty is also reported. Left: ν_e spectrum; right: ν_μ spectrum.

range [100 MeV - 10 GeV], usually referred to as "low-energy" region. The flux reconstructed in this work shows the good capabilities of a large LS-based detector like JUNO to measure the atmospheric neutrino flux. The energy region considered is already populated by other measurements, but some discrepancies survive. JUNO can provide additional information about an interesting energy region, also helping models in constraining their predictions. The quoted uncertainty is competitive with present experimental results, with a significative margin of improvement given by the increasing of exposure time. Altough the JUNO design is not optimized for the atmospheric neutrino physics, due to both the lack of statistics and to the inability of reconstructing single-particle directions (e.g. with respect to Super-Kamiokande), the extremely good performances in the atmospheric neutrino energy reconstruction can be fully exploited for the measurement of the energy spectrum.
Moreover, the atmospheric neutrino flux is a natural source which will be fully accessible from the beginning of data taking.

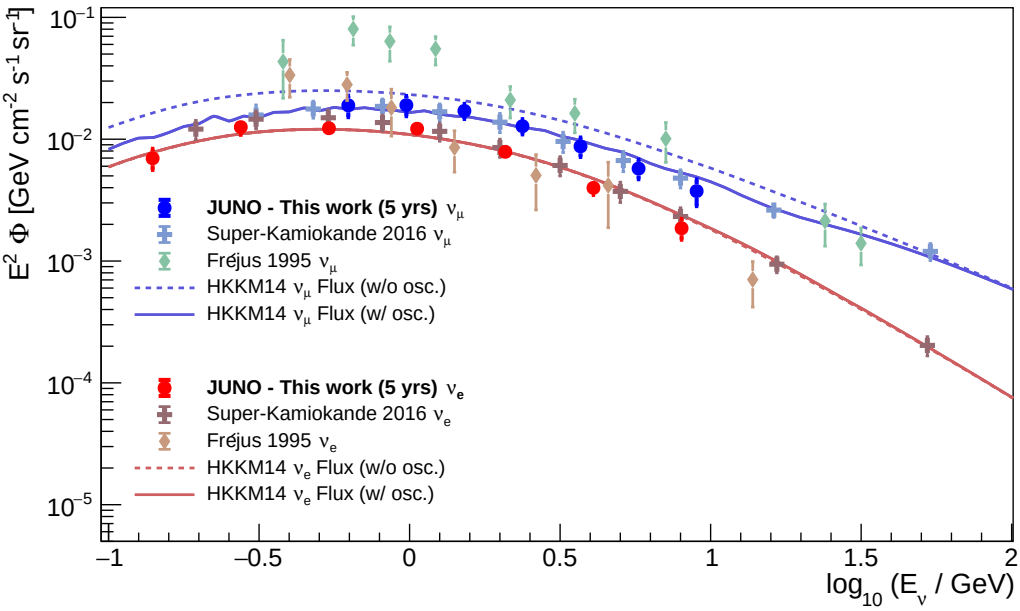

Figure 6.10: Atmospheric neutrino energy spectra reconstructed in this work for ν_e and ν_μ, compared with present measurements in the same energy region. The fluxes measured by Super-Kamiokande [45] and Fréjus [37] are reported. The HKKM14 [34] model predictions are also reported, both at the source and including oscillation effects. The fluxes are multiplied by E^2, to give a better picture.

Conclusions

The JUNO detector represents a wide-community effort in pushing the current knowledge in fundamental physics to the very edge. The unprecedented resolution which is necessary to achieve requires a simultaneous control of many aspects, both from the engineering and the physics side. The detector will be ready in two years and is planned to be active for at least two decades. JUNO has been designed from the beginning as a state-of-art detector for the MeV neutrino physics. The goal of determining the mass ordering above 3σ is an ambitious challenge, which the collaboration is addressing from many sides. Most of the effort is devoted to the tuning of all parameters, in order to allow an extremely precise reconstruction of the reactor neutrino spectrum and observe with a sufficient significance the tiny structures which point to the true ordering. The large dimensions of the detector, as well as its dense instrumentation, pave the way to all a series of other measurements, in a multi-purpose approach. The atmospheric neutrino flux is a natural source that can be observed, from the very beginning of the data-taking. Although the detector design is not optimized for this class of events, the large active volume and the fine energy resolution allow to reconstruct the energy spectrum with a competitive precision, especially in the low-energy region.
In this work, a large set of MC events has been generated, to evaluate the detector performances. A smaller set has been used to simulate the real data. Thanks to the timing performances of JUNO, the flavor of primary neutrinos can be separated, with a limited residual contamination. The atmospheric neutrino energy spectrum has been reconstructed in the energy range [100 MeV - 10 GeV], separately for ν_e and ν_μ, assuming a $\sim$5 years detector livetime. The reconstructed spectra lie inside an interesting energy region, where previous measurements show some discrepancies. The results obtained show the potential of JUNO in pushing the atmospheric flux measurements through the multi-MeV region, so far not covered by past experiments and where theoretical models have large uncertainties. The information inferred can provide a fruitful input to constrain flux predictions, which are essential to evaluate the atmospheric neutrino flux impact in the search of rare events.

Bibliography

[1] W. Pauli. Letter to the "radioactives" in Tubingen, december 1930. *Cambridge Monogr. Part. Phys. Nucl. Phys. Cosmol.*, 14:1, 2000.

[2] E. Fermi. Versuch einer theorie der β-strahlen. i. *Zeitschrift für Physik*, 88(3):161–177, 1934.

[3] J Chadwick. Possible existence of a neutron. *Nature*, 129(312), 1932.

[4] M. Tanabashi et al. Review of Particle Physics. *Phys. Rev. D*, 98:030001, 2018.

[5] C. Giunti and C. W. Kim. *Fundamentals of neutrino physics and astrophysics*. Oxford University Press, 2007.

[6] O. Klein. Mesons and nucleons. *Nature*, 161:897–899, 1948.

[7] F. Mandl and G. Shaw. *Quantum Field Theory*. Wiley, 2 edition, 2013.

[8] T. D. Lee and C. N. Yang. Question of parity conservation in weak interactions. *Phys. Rev.*, 104:254–258, 1956.

[9] C. S. Wu, E. Ambler, R. W. Hayward, D. D. Hoppes, and R. P. Hudson. Experimental test of parity conservation in beta decay. *Phys. Rev.*, 105:1413–1415, 1957.

[10] M. Goldhaber, L. Grodzins, and A. W. Sunyar. Helicity of neutrinos. *Phys. Rev.*, 109:1015–1017, 1958.

[11] I. Ostrovskiy and K. O'Sullivan. Search for neutrinoless double beta decay. *Modern Physics Letters A*, 31(18):1630017, 2016.

[12] S. Weinberg. A model of leptons. *Phys. Rev. Lett.*, 19:1264–1266, 1967.

[13] A. Salam. Weak and Electromagnetic Interactions. *Conf. Proc.*, C680519:367–377, 1968.

[14] S. L. Glashow. Partial-symmetries of weak interactions. *Nuclear Physics*, 22(4):579 – 588, 1961.

[15] F.J. Hasert et al. Search for elastic muon-neutrino electron scattering. *Physics Letters B*, 46(1):121 – 124, 1973.

[16] F.J. Hasert et al. Observation of neutrino-like interactions without muon or electron in the Gargamelle neutrino experiment. *Physics Letters B*, 46(1):138 – 140, 1973.

[17] F.J. Hasert et al. Observation of neutrino-like interactions without muon or electron in the Gargamelle neutrino experiment. *Nuclear Physics B*, 73(1):1 – 22, 1974.

[18] P. W. Higgs. Broken symmetries and the masses of gauge bosons. *Phys. Rev. Lett.*, 13:508–509, 1964.

[19] F. Englert and R. Brout. Broken symmetry and the mass of gauge vector mesons. *Phys. Rev. Lett.*, 13:321–323, 1964.

[20] G. S. Guralnik, C. R. Hagen, and T. W. B. Kibble. Global conservation laws and massless particles. *Phys. Rev. Lett.*, 13:585–587, 1964.

[21] C. L. Cowan, F. Reines, F. B. Harrison, H. W. Kruse, and A. D. McGuire. Detection of the free neutrino: a confirmation. *Science*, 124(3212):103–104, 1956.

[22] C.V. Achar et al. Detection of muons produced by cosmic ray neutrinos deep underground. *Physics Letters*, 18(2):196 – 199, 1965.

[23] F. Reines et al. Evidence for high-energy cosmic-ray neutrino interactions. *Phys. Rev. Lett.*, 15:429–433, 1965.

[24] J. A. Formaggio and G. P. Zeller. From ev to Eev: Neutrino cross sections across energy scales. *Rev. Mod. Phys.*, 84:1307–1341, 2012.

[25] B. Pontecorvo. Neutrino experiments and the problem of conservation of leptonic charge. *Journal of Experimental and Theoretical Physics*, 26:984–988, 1968.

[26] Z. Maki, M. Nakagawa, and S. Sakata. Remarks on the Unified Model of Elementary Particles. *Progress of Theoretical Physics*, 28(5):870–880, 1962.

[27] X. Qian and P. Vogel. Neutrino mass hierarchy. *Progress in Particle and Nuclear Physics*, 83:1 – 30, 2015.

[28] L. Wolfenstein. Neutrino oscillations in matter. *Phys. Rev. D*, 17:2369–2374, 1978.

[29] S. P. Mikheyev and A. Yu Smirnov. Resonance Amplification of Oscillations in Matter and Spectroscopy of Solar Neutrinos. *Soviet Journal of Nuclear Physics*, 42:913–917, 1985. [,305(1986)].

[30] R. Enberg, M. H. Reno, and I. Sarcevic. Prompt neutrino fluxes from atmospheric charm. *Phys. Rev. D*, 78:043005, 2008.

[31] M. Honda, T. Kajita, K. Kasahara, and S. Midorikawa. New calculation of the atmospheric neutrino flux in a three-dimensional scheme. *Phys. Rev. D*, 70:043008, 2004.

[32] M. Honda, T. Kajita, K. Kasahara, S. Midorikawa, and T. Sanuki. Calculation of atmospheric neutrino flux using the interaction model calibrated with atmospheric muon data. *Phys. Rev. D*, 75:043006, 2007.

[33] M. Honda, T. Kajita, K. Kasahara, and S. Midorikawa. Improvement of low energy atmospheric neutrino flux calculation using the JAM nuclear interaction model. *Phys. Rev. D*, 83:123001, 2011.

[34] M. Honda, M. Sajjad Athar, T. Kajita, K. Kasahara, and S. Midorikawa. Atmospheric neutrino flux calculation using the NRLMSISE-00 atmospheric model. *Phys. Rev. D*, 92:023004, 2015.

[35] G. Battistoni, A. Ferrari, T. Montaruli, and P.R. Sala. The FLUKA atmospheric neutrino flux calculation. *Astroparticle Physics*, 19(2):269 – 290, 2003.

[36] G. D. Barr, T. K. Gaisser, P. Lipari, S. Robbins, and T. Stanev. Three-dimensional calculation of atmospheric neutrinos. *Phys. Rev. D*, 70:023006, 2004.

[37] K. Daum et al. Determination of the atmospheric neutrino spectra with the Fréjus detector. *Zeitschrift für Physik C Particles and Fields*, 66(3):417–428, 1995.

[38] M Aglietta et al. Experimental study of upward stopping muons in NUSEX. *Europhysics Letters (EPL)*, 15(5):559–564, 1991.

[39] R. Becker-Szendy et al. Electron- and muon-neutrino content of the atmospheric flux. *Phys. Rev. D*, 46:3720–3724, 1992.

[40] Y. Fukuda et al. Atmospheric $\nu_\mu\nu_e$ ratio in the multi-GeV energy range. *Physics Letters B*, 335(2):237 – 245, 1994.

[41] R. Abbasi et al. Determination of the atmospheric neutrino flux and searches for new physics with AMANDA-II. *Phys. Rev. D*, 79:102005, 2009.

[42] R. Abbasi et al. The energy spectrum of atmospheric neutrinos between 2 and 200tev with the AMANDA-II detector. *Astroparticle Physics*, 34(1):48 – 58, 2010.

[43] W.W.M. Allison et al. Measurement of the atmospheric neutrino flavour composition in Soudan 2. *Physics Letters B*, 391(3):491 – 500, 1997.

[44] F. Ronga. Atmospheric neutrino induced muons in the MACRO detector. *Nuclear Physics B - Proceedings Supplements*, 77(1):117 – 122, 1999.

[45] E. Richard et al. Measurements of the atmospheric neutrino flux by Super-Kamiokande: Energy spectra, geomagnetic effects, and solar modulation. *Phys. Rev. D*, 94:052001, 2016.

[46] S. Adrián-Martínez et al. Measurement of the atmospheric ν_μ energy spectrum from 100 Gev to 200 Tev with the ANTARES telescope. *The European Physical Journal C*, 73(10):2606, 2013.

[47] R. Abbasi et al. Measurement of the atmospheric neutrino energy spectrum from 100 Gev to 400 Tev with IceCube. *Phys. Rev. D*, 83:012001, 2011.

[48] M. G. Aartsen et al. Measurement of the atmospheric ν_e flux in IceCube. *Phys. Rev. Lett.*, 110:151105, 2013.

[49] M. G. Aartsen et al. Measurement of the atmospheric ν_e spectrum with IceCube. *Phys. Rev. D*, 91:122004, 2015.

[50] M. G. Aartsen et al. Development of a general analysis and unfolding scheme and its application to measure the energy spectrum of atmospheric neutrinos with IceCube. *The European Physical Journal C*, 75(3):116, 2015.

[51] M. G. Aartsen et al. Measurement of the ν_μ energy spectrum with IceCube-79. *The European Physical Journal C*, 77(10):692, 2017.

[52] Ch. Berger et al. The Fréjus nucleon decay detector. *Nuclear Instruments and Methods in Physics Research Section A: Accelerators, Spectrometers, Detectors and Associated Equipment*, 262(2):463 – 495, 1987.

[53] S. Fukuda et al. The Super-Kamiokande detector. *Nuclear Instruments and Methods in Physics Research Section A: Accelerators, Spectrometers, Detectors and Associated Equipment*, 501(2):418 – 462, 2003.

[54] Y. Fukuda et al. Evidence for oscillation of atmospheric neutrinos. *Phys. Rev. Lett.*, 81:1562–1567, 1998.

[55] M. Ageron et al. ANTARES: The first undersea neutrino telescope. *Nuclear Instruments and Methods in Physics Research Section A: Accelerators, Spectrometers, Detectors and Associated Equipment*, 656(1):11 – 38, 2011.

[56] M. G. Aartsen and others (IceCube Collaboration). Evidence for high-energy extraterrestrial neutrinos at the IceCube Detector. *Science*, 342(6161), 2013.

[57] R. Abbasi et al. IceTop: The surface component of IceCube. *Nuclear Instruments and Methods in Physics Research Section A: Accelerators, Spectrometers, Detectors and Associated Equipment*, 700:188 – 220, 2013.

[58] F. An et al. Neutrino physics with JUNO. *Journal of Physics G: Nuclear and Particle Physics*, 43(3):030401, 2016.

[59] Z. Djurcic et al. JUNO Conceptual Design Report. 2015.

[60] P. Lombardi et al. Distillation and stripping pilot plants for the JUNO neutrino detector: Design, operations and reliability. *Nuclear Instruments and Methods in Physics Research Section A: Accelerators, Spectrometers, Detectors and Associated Equipment*, 925:6 – 17, 2019.

[61] Q. Zhang. The JUNO calibration complex and its simulation. *Poster presented at the 2019 International Conference on Computing in High Energy & Nuclear Physics*, 2019.

[62] R. Wang, H. Lu, and C. Yang. Water cherenkov detector of the JUNO veto system. *Poster presented at the 2019 EPS Conference on High Energy Physics*, 2019.

[63] T. Adam et al. The OPERA experiment Target Tracker. *Nuclear Instruments and Methods in Physics Research Section A: Accelerators, Spectrometers, Detectors and Associated Equipment*, 577(3):523 – 539, 2007.

[64] H. Zhang. Tested performance of JUNO 20"pmts. *Poster presented at the 2018 Neutrino Conference*, 2018.

[65] A. Tietzsch. The pmt mass testing system for JUNO. *Poster presented at the 2018 Neutrino Conference*, 2018.

[66] Y. Han. Stereo Calorimetry in JUNO: Physics Motivation and Instrumentation. *Poster presented at the 2018 Neutrino Conference*, 2018.

[67] B. Z. Hu and J. Xu. The 3-inch pmts of the JUNO experiment. *Poster presented at 2018 Neutrino Conference*, 2018.

[68] B. Asavapibhop. Earth Magnetic Field Compensation Coils System for JUNO. *Poster presented at the 2018 Neutrino Conference*, 2018.

[69] C. Yanagisawa and T. Kato. Report on the super-kamiokande accident. Technical report, University of Tokio, 2001.

[70] M. Xu. Implosion protection and waterproof potting for the JUNO 20-inch PMTs. *Poster presented at the 2018 International Conference on High Energy Physics*, 2018.

[71] F. Marini. The JUNO large PMT readout electronics. *Poster presented at the 2019 International Workshop on Weak Interactions and Neutrinos*, 2019.

[72] C. Andreopoulos et al. The GENIE neutrino Monte Carlo generator. *Nuclear Instruments and Methods in Physics Research Section A: Accelerators, Spectrometers, Detectors and Associated Equipment*, 614(1):87 – 104, 2010.

[73] R. Brun and F. Rademakers. ROOT - an object oriented data analysis framework. *Nuclear Instruments and Methods in Physics Research Section A: Accelerators, Spectrometers, Detectors and Associated Equipment*, 389(1):81 – 86, 1997. New Computing Techniques in Physics Research V.

[74] D. G. Michael et al. Observation of Muon Neutrino Disappearance with the MINOS Detectors in the NuMI Neutrino Beam. *Phys. Rev. Lett.*, 97:191801, 2006.

[75] L. Fields et al. Measurement of Muon Antineutrino Quasielastic Scattering on a Hydrocarbon Target at $E_\nu \sim 3.5\,GeV$. *Phys. Rev. Lett.*, 111:022501, 2013.

[76] K. Abe et al. The T2K experiment. *Nuclear Instruments and Methods in Physics Research Section A: Accelerators, Spectrometers, Detectors and Associated Equipment*, 659(1):106 – 135, 2011.

[77] P. Adamson et al. First measurement of muon-neutrino disappearance in NOvA. *Phys. Rev. D*, 93:051104, 2016.

[78] A. Bodek and J. L. Ritchie. Further studies of Fermi-motion effects in lepton scattering from nuclear targets. *Phys. Rev. D*, 24:1400–1402, 1981.

[79] J.J. Aubert et al. The ratio of the nucleon structure functions F2N for iron and deuterium. *Physics Letters B*, 123(3):275 – 278, 1983.

[80] A Bodek and U K Yang. Higher twist, ξ_w scaling, and effective LO PDFs for lepton scattering in the few GeV region. *Journal of Physics G: Nuclear and Particle Physics*, 29(8):1899–1905, 2003.

[81] C.H. Llewellyn Smith. Neutrino reactions at accelerator energies. *Physics Reports*, 3(5):261 – 379, 1972.

[82] L. A. Ahrens et al. Measurement of neutrino-proton and antineutrino-proton elastic scattering. *Phys. Rev. D*, 35:785–809, 1987.

[83] D. Rein and L. M Sehgal. Neutrino-excitation of baryon resonances and single pion production. *Annals of Physics*, 133(1):79 – 153, 1981.

[84] D. Rein and L. M. Sehgal. Coherent π^0 production in neutrino reactions. *Nuclear Physics B*, 223(1):29 – 44, 1983.

[85] D. Rein and L.M. Sehgal. PCAC and the deficit of forward muons in π^+ production by neutrinos. *Physics Letters B*, 657(4):207 – 209, 2007.

[86] D. Akimov et al. Observation of coherent elastic neutrino-nucleus scattering. *Science*, 357(6356):1123–1126, 2017.

[87] W. J Marciano and Z. Parsa. Neutrino–electron scattering theory. *Journal of Physics G: Nuclear and Particle Physics*, 29(11):2629–2645, 2003.

[88] J. H. Zou et al. SNiPER: an offline software framework for non-collider physics experiments. *Journal of Physics: Conference Series*, 664(7):072053, 2015.

[89] S. Agostinelli et al. Geant4-a simulation toolkit. *Nuclear Instruments and Methods in Physics Research Section A: Accelerators, Spectrometers, Detectors and Associated Equipment*, 506(3):250 – 303, 2003.

[90] V. Ivanchenko et al. Recent Improvements in Geant4 Electromagnetic Physics Models and Interfaces. *Progress in NUCLEAR SCIENCE and TECHNOLOGY*, 2:898–903, 2011.

[91] J. Allison et al. Recent developments in Geant4. *Nuclear Instruments and Methods in Physics Research Section A: Accelerators, Spectrometers, Detectors and Associated Equipment*, 835:186 – 225, 2016.

[92] G. Settanta et al. e-μ discrimination at high energy in the JUNO detector. *EPJ Web Conf.*, 209:01011, 2019.

[93] M. Guan et al. A parametrization of the cosmic-ray muon flux at sea-level, 2015.

[94] V.A. Kudryavtsev. Muon simulation codes MUSIC and MUSUN for underground physics. *Computer Physics Communications*, 180(3):339 – 346, 2009.

[95] K. Abe et al. Search for proton decay via $p \to e^+\pi^0$ and $p \to \mu^+\pi^0$ in 0.31 megaton $\cdot$ years exposure of the Super-Kamiokande water Cherenkov detector. *Phys. Rev. D*, 95:012004, 2017.

[96] G. D'Agostini. A multidimensional unfolding method based on Bayes' theorem. *Nuclear Instruments and Methods in Physics Research Section A: Accelerators, Spectrometers, Detectors and Associated Equipment*, 362(2):487 – 498, 1995.

[97] G. D'Agostini. Improved iterative Bayesian unfolding, 2010.

[98] C. Andreopoulos et al. The GENIE Neutrino Monte Carlo Generator: Physics and User Manual. 2015.

[99] K. Abe et al. Measurement of the Inclusive Electron Neutrino Charged Current Cross Section on Carbon with the T2K Near Detector. *Phys. Rev. Lett.*, 113:241803, 2014.

[100] K. Abe et al. Measurement of the ν_μ charged-current quasielastic cross section on carbon with the ND280 detector at T2K. *Phys. Rev. D*, 92:112003, 2015.

[101] K. Abe et al. First measurement of the muon neutrino charged current single pion production cross section on water with the T2K near detector. *Phys. Rev. D*, 95:012010, 2017.

[102] E. Richard. *Studies of the energy, azimuthal, and time spectra of the atmospheric neutrino flux at Super-Kamiokande*. PhD thesis, University of Tokyo, 2015.

Acknowledgements

I would like to thank Prof. Stefano Mari for the supervision of this thesis and, in a wider view, for having guided me throughout my university path. I am grateful to Paolo Montini, who helped me in many circumstances and gave me fruitful suggestions along all this thesis work. I would like to thank the JUNO Collaboration, for the feedback received during the development of this thesis. I would also like to thank the Computing Group of my department, for the support activity in any trouble with the local cluster.
I am finally grateful to my family, without whom I wouldn't had the opportunity to grow in the Science world.